
A MARKOVIAN VIEW OF ITERATIVE-FEEDBACK LOOPS IN IMAGE GENERATIVE MODELS: NEURAL RESONANCE AND MODEL COLLAPSE

Vibhas Kumar Vats¹, David J. Crandall¹, samuel Goree²

¹ Luddy School of Informatics, Computing, and Engineering, Indiana University, Bloomington, IN, USA

² Department of Computer Science, Stonehill College, Easton, MA, USA

ABSTRACT

AI training datasets will inevitably contain AI-generated examples, leading to “feedback” in which the output of one model impacts the training of another. It is known that such iterative feedback can lead to model collapse, yet the mechanisms underlying this degeneration remain poorly understood. Here we show that a broad class of feedback processes converges to a low-dimensional invariant structure in latent space, a phenomenon we call *neural resonance*. By modeling iterative feedback as a Markov Chain, we show that two conditions are needed for this resonance to occur: *ergodicity* of the feedback process and *directional contraction* of the latent representation. By studying diffusion models on MNIST and ImageNet, as well as CycleGAN and an audio feedback experiment, we map how local and global manifold geometry evolve, and we introduce an eight-pattern taxonomy of collapse behaviors. Neural resonance provides a unified explanation for long-term degenerate behavior in generative models and provides practical diagnostics for identifying, characterizing, and eventually mitigating collapse.

Keywords: self-training loops; iterative-feedback loops; generational Markov chain; neural resonance; model collapse.

1 Introduction

Generative AI models are now so widely used that the text, imagery, audio, and video that they create will inevitably “pollute” the training datasets of the next generation of models — and those models, in turn, will pollute the training datasets of the subsequent generation, and so on. This can create an iterative feedback loop, causing training sets to co-evolve with subsequent generations of models [1] and drift away from the true data distribution they were meant to represent.

Recent work has shown that such feedback can eventually lead to “model collapse” [2], with potentially catastrophic implications for modern AI systems. However, the underlying dynamics of iterative feedback leading to model collapse are poorly understood. For example, do generative models undergoing iterative feedback behave chaotically, or do they converge to predictable stable points? Do distributions of latent representations contract or expand, do semantic modes survive or decay, and does generational drift reach a stable point or does it continue forever?

Of course, systems undergoing iterative feedback are nothing new. To study latent feedback in AI models, we were inspired by a work of sonic art. In 1969, Alvin Lucier’s avant-garde composition *I Am Sitting in a Room* [3] interrogates similar concepts. In it, Lucier speaks several sentences into a tape recorder explaining his process, and then plays it back in his Connecticut apartment while re-recording it on a second device. While the first recording faithfully captures the words and his voice, after multiple iterations the sound of his speech dissolves into tones that have more to do with the geometry of the room and the noise characteristics of the equipment than what he actually said. This degradation process can be well explained by physical laws that govern how transformations affect audio signals over time. We wondered: are there similar principles that explain how AI models will react to iterative feedback?

In this paper we show, for the first time, that many generative feedback processes follow a surprisingly predictable long-term behavior. Across several diverse model classes, including diffusion models trained on their own outputs, deep

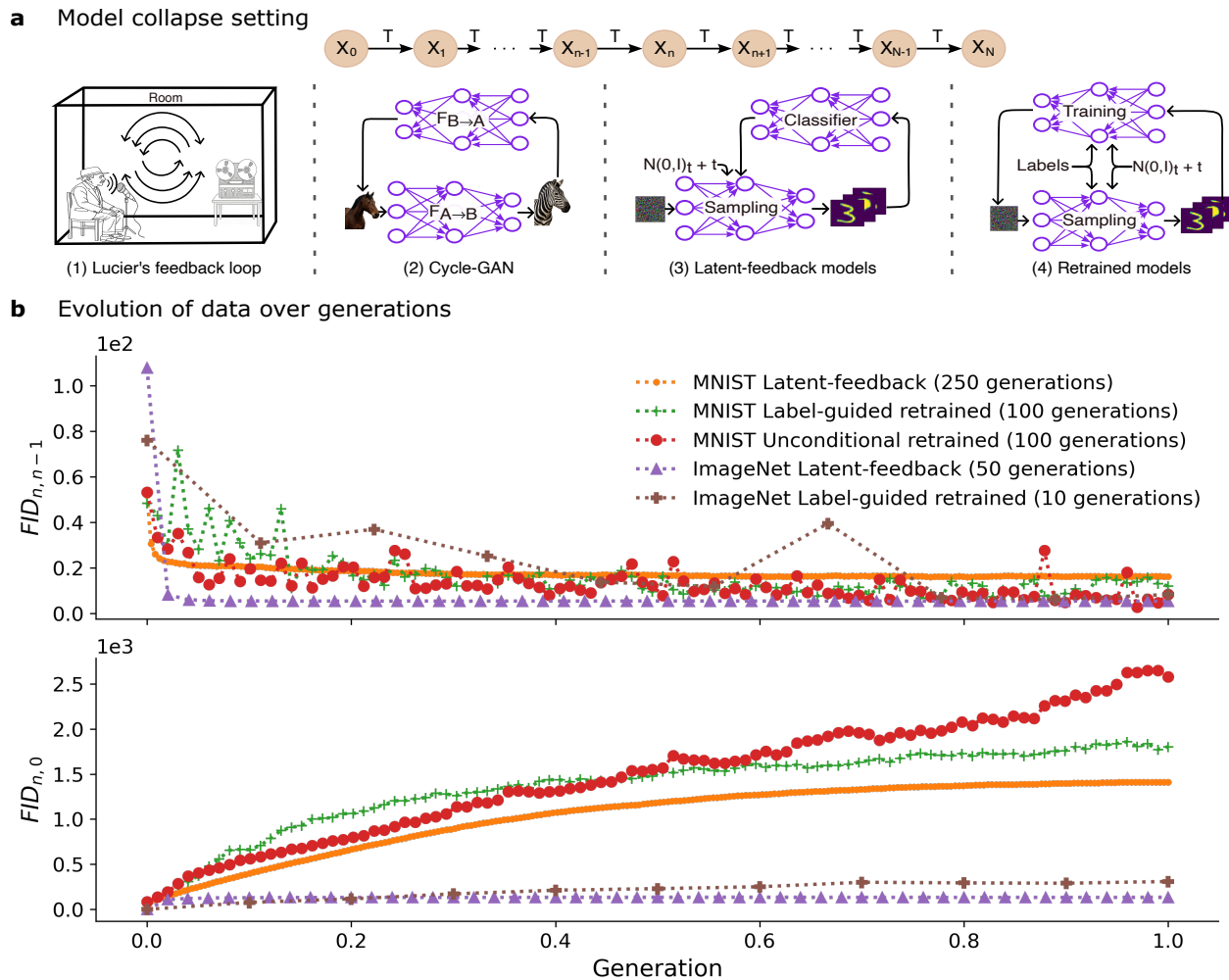


Figure 1: **A high-level representation of the Iterative feedback process.** (a) A graphical representation of the generational Markov chain and cartoon overview of our iterative generation settings. X_n represents the current distribution of images at generation n . (b) Data distribution distances for two experiments in scenario (3), and three experiments in scenario (4), measured using FID score. The top plot shows single-step changes between consecutive generations, while the bottom plot shows cumulative change from the original distribution. Experimental runs with differing numbers of generations are scaled to the width of the graph, so that the x-axis represents fraction of total generations, and each point is one generation.

style transfer models applied repeatedly on the same image, and even Lucier’s sonic art piece, we find that iterative feedback often pushes the latent representation toward a low-dimensional invariant structure. We call this phenomenon *neural resonance*, in analogy to resonance in physical systems in which repeatedly-applied transformations can cause some modes to be amplified while others are suppressed.

To characterize neural resonance and how it arises, we model iterative feedback as a Markov Chain, choosing states and transitions depending on the feedback situation to be modeled. Using this general framework, we identify two conditions that are needed for resonance to emerge: *ergodicity*, meaning that the chain converges to a unique stationary distribution that is independent of the initial state [4], and *directional contraction*, in which latent features shrink towards a progressively smaller set of axes. Under these conditions, the system exhibits two distinct phases: an initial *transient* phase when the distribution changes rapidly from one iteration to the next, followed by a *stationary* phase in which the distribution remains essentially unchanged. When either condition fails, the latent features expand and the system does not exhibit neural resonance (Table 2).

We introduce simple diagnostic measures for identifying resonance, based on complementary measures of local and cumulative drift between iterations. We introduce a compact eight-pattern taxonomy of semantic expansion and

contraction behaviors (Table 1) that describes how local and global latent geometry evolve under feedback. Applying the taxonomy across different types of feedback with different datasets shows that data compressibility strongly influences the outcome: highly compressible datasets such as MNIST keep their semantics over generations, whereas more diverse datasets like ImageNet lose semantics and collapse into very simple examples.

Taken together, our results provide a framework for understanding the dynamics of generative feedback, including model collapse. Neural resonance explains why collapse occurs, how long-term latent structures stabilize, and why models trained on diverse real data are likely to outperform models trained on synthetic images. Our findings also suggest practical diagnostic tools for monitoring and mitigating degeneration caused by iterative feedback, which may be essential in future AI systems as synthetic data becomes increasingly common.

2 Iterative Feedback as a Markov Chain

We model the iterative feedback process as a Markov Chain [4]. We consider two main types of iterative feedback. First, we consider feedback that is at the image or sample level: a single image that is transformed back and forth using CycleGAN, for example, or the audio signal that is iteratively transformed in Lucier’s piece. In the first case, the state space of the Markov Chain consists of all possible images. Starting from an initial input image X_0 , each iteration of feedback is modeled as an operator $T(\cdot)$ which produces $X_{n+1} = T(X_n)$ (see Fig. 1a). Second, we consider when the feedback is instead at the dataset level, such as a model that is trained on its own previous outputs. In this case, the state space conceptually consists of all possible dataset distributions, and the system moves from state to state to describe how distributions evolve across successive generations. Importantly, in either case, the process obeys the Markov property that future states (images or data distributions) depend only on the current state, not the full history.

If a Markov Chain is ergodic, it converges to a unique stationary distribution, regardless of the initial state (see §3 of Supplementary for in-depth discussion). In our context, this corresponds to when the distribution of generated images stabilizes such that images X_{n+1} and X_n are drawn from statistically indistinguishable distributions. In practice, this often means that the images generated by subsequent iterations become very similar to one another. To quantify convergence in Markov Chains, we monitor two complementary measures of drift using Fréchet Inception Distances (FID): the local drift, $FID_{n,n-1}$, and the cumulative drift, $FID_{n,0}$, as shown in Fig. 1-b. When both curves plateau, the process is considered to have reached *empirical stationarity*, meaning the change in FID score from one generation to the next is less than some tolerance ϵ . Fig. 1-b shows the local drift $FID_{n,n-1}$ (top) and the cumulative drift $FID_{n,0}$ (bottom) for three Markov Chains—latent-feedback (conditioned on latent image representations), label-guided retrained (conditioned on class labels), and unconditional-retrained (no conditionals)—evaluated on MNIST and ImageNet-5. For MNIST, FID scores are computed in the latent space of a locally trained classifier, while for ImageNet-5 they are computed in the Inception-V3 feature space. Across all settings, local drift decreases rapidly and stabilizes, while cumulative drift rises and then saturates for the latent-feedback and label-guided retrained chains, yielding a joint plateau that signifies empirical stationarity. By contrast, the unconditional-retrained chain exhibits persistent local and cumulative drift across all 100 generations, indicating that it has not yet reached stationarity. The corresponding evolution of class exemplars is shown in Fig. 2(a-e).

3 Neural Resonance

The convergence of a Markov Chain toward a stationary distribution mirrors the acoustic phenomenon in Alvin Lucier’s piece *I Am Sitting in a Room*. In that work, each re-recording applies the room’s linear transfer operator: frequencies misaligned with the dominant eigenmodes decay exponentially, leaving only the resonant ‘room chord.’ This process illustrates a general rule: when a transformation is repeated, the system selectively amplifies the modes it can sustain. An analogous mechanism unfolds in neural network-based generative feedback systems. In an ergodic Markov Chain, which converges to a unique stationary distribution independent of initialization, repeated application of the feedback operator T filters the latent representation, damping off-manifold directions and preserving modes aligned with the invariant manifold. Ergodicity ensures that the Markov Chain eventually forgets its initialization and converges toward a stationary distribution confined to a contracted region of the latent manifold. Contraction implies that most representational axes in this space are progressively attenuated under feedback, while a small subset persists across generations. Iterative feedback thus concentrates representations onto this invariant subset, analogous to physical resonance. When this Lucier-like selective convergence appears within a fixed latent feature space, we refer to it as *neural resonance*.

Two conditions are jointly necessary to observe neural resonance: *directional contraction* and *ergodic Markov Chains*. Directional contraction shapes the geometric limit of the latent manifold by progressively shrinking and organizing its representation, thereby stabilizing the manifold’s effective degrees of freedom across generations. As in Lucier’s

Table 1: **Latent-manifold dynamics under neural resonance.** Each row lists a distinct combination of directional change in the local spread (σ_{intra}), the local curvature measure (m_{LB}), and the global participation ratio (PR_G). Patterns are grouped into two regimes, semantic expansion ($\sigma_{intra} \uparrow$) and semantic contraction ($\sigma_{intra} \downarrow$), and each is labeled according to its geometric character (e.g., coherent expansion, wrinkled contraction). An animation illustrating these patterns is provided in the Supplementary Video.

| Manifold Behavior | | Local Metrics | | Global Metric | Dimensional Pattern |
|------------------------------------|-------------|------------------|--------------|---------------|------------------------------|
| Local | Global | σ_{intra} | m_{LB} | PR_G | |
| Semantic Expansion Regime | | | | | |
| Expansion | Expansion | \uparrow | \uparrow | \uparrow | Coherent Expansion (CE) |
| Expansion | Contraction | \uparrow | \uparrow | \downarrow | Wrinkled Expansion (WE) |
| Expansion | Expansion | \uparrow | \downarrow | \uparrow | Anisotropic Expansion (AE) |
| Expansion | Contraction | \uparrow | \downarrow | \downarrow | Oblate Expansion (OE) |
| Semantic Contraction Regime | | | | | |
| Contraction | Contraction | \downarrow | \downarrow | \downarrow | Coherent Contraction (CC) |
| Contraction | Expansion | \downarrow | \downarrow | \uparrow | Anisotropic Contraction (AC) |
| Contraction | Contraction | \downarrow | \uparrow | \downarrow | Wrinkled Contraction (WC) |
| Contraction | Expansion | \downarrow | \uparrow | \uparrow | Oblate Contraction (OC) |

piece, repeated playback preferentially reinforces the room’s resonant frequencies until they dominate across iterations. Similarly, in ergodic Markov Chains, directional contraction selects latent modes while ergodicity sustains them, as exemplified by latent-feedback, label-guided retrained and unconditional retrained models. By contrast, in non-ergodic Markov Chains, iterative feedback can select modes without sustaining them. Deterministic or weak-noise feedback loops (e.g., CycleGAN) exemplify this behavior.

3.1 Latent Manifold Dynamics

We characterize latent-manifold dynamics in terms of dimensionality using two complementary metrics: the participation ratio, PR_G , which tracks global dimensionality; and the Levina-Bickel intrinsic dimension [5], m_{LB} , which tracks local dimensionality. We also use intra-class spread, σ_{intra} , measuring classwise dispersion, to observe local expansion and contraction. Under iterative feedback, components orthogonal to the eventual invariant subspace are progressively damped, and thus PR_G contracts and stabilizes at a floor reflecting the dimension of that subspace. Within that emerging subspace, local structure can still reconfigure—both m_{LB} and σ_{intra} may transiently rise or fall before settling—without undoing the global contraction.

We characterize changes in the latent manifold by examining metric trajectories across generations. Taken together, PR_G (global) and m_{LB} (local) delineate eight dimensional patterns that summarize how local and global manifold geometry co-evolve under feedback (see Table 1); σ_{intra} indicates local expansion versus contraction regimes. These patterns form pairs, where one pattern is the opposite of another. These patterns are not always intuitive; physical analogies, together with Supplementary video animation, clarify them.

- *Coherent expansion (CE)*. $\sigma_{intra} \uparrow$ activates new axes locally and globally: $PR_G \uparrow$, $m_{LB} \uparrow$. The manifold simultaneously puffs out and unfolds, like an inflating balloon. *Coherent contraction (CC)* is the reverse.
- *Oblate expansion (OE)*. $\sigma_{intra} \uparrow$ along one or a few dominant directions while collapsing elsewhere: $PR_G \downarrow$, $m_{LB} \downarrow$. The manifold flattens and spreads along a few axes, like a balloon squeezed between hands, expanded sideways along a few axes while collapsed along others. *Oblate contraction (OC)* is the reverse.
- *Wrinkled expansion (WE)*. $\sigma_{intra} \uparrow$ forms small-scale wrinkles or folds: $m_{LB} \uparrow$ while $PR_G \downarrow$. The manifold fans out locally as fine wrinkles form, reducing global spread, like crumpled fabric with wrinkles. *Anisotropic contraction (AC)* is the reverse.
- *Anisotropic expansion (AE)*. $\sigma_{intra} \uparrow$ stretches clusters along different axes: $m_{LB} \downarrow$, $PR_G \uparrow$. Local structure collapses along stretched directions while new global axes are activated, like multiple pieces of play-dough being stretched in different directions, each elongating along its own axis while globally occupying a larger space. *Wrinkled contraction (WC)* is the reverse.

Table 2: Summary of observed latent manifold dynamics with sparkline plots. The dynamics is indicated with Coherent Expansion (CE), Wrinkled Expansion (WE), Oblate Expansion (OE), Coherent Contraction (CC), and Wrinkled Contraction (WC). LGR and LF means label-guided retrained and latent-feedback models, respectively. CycleGAN experiment uses Horse-Zebra data. See Supplementary Materials for full plots with axes.

| Experiments | σ_{intra} | m_{LB} | PR_G | Dynamics |
|---------------|------------------|----------|--------|----------|
| LGR-MNIST | | | | CC→WC |
| LF-MNIST | | | | OE |
| LGR-ImageNet5 | | | | CC |
| LF-ImageNet5 | | | | WE |
| CycleGAN | | | | CE |

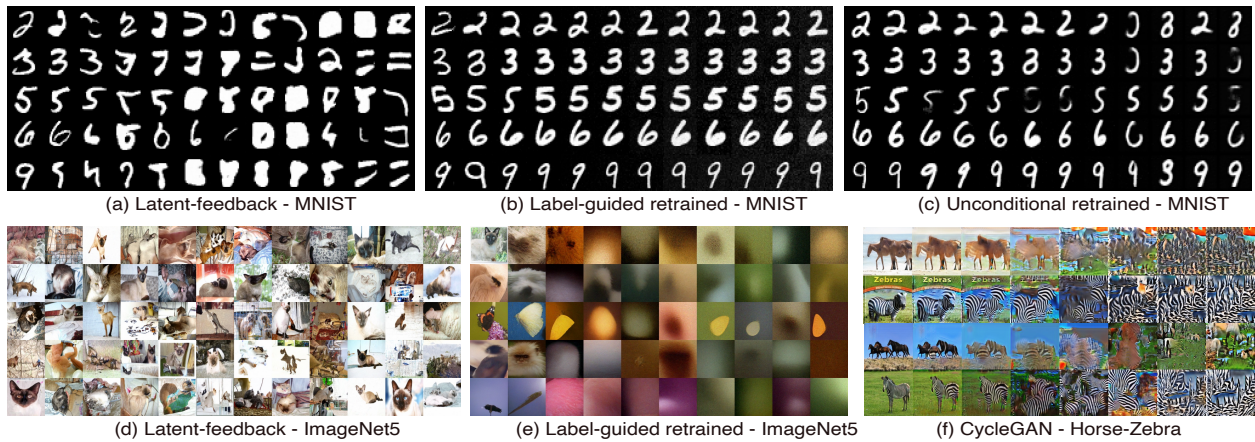


Figure 2: **Evolution of class exemplars under iterative feedback.** Columns: same-generation samples. (a–c) MNIST: latent-feedback progressively loses semantic coherence; label-guided and unconditional retraining retain class identity but converge to repetitive templates owing to high compressibility. (d–e) ImageNet-5: both regimes collapse, but differently: latent-feedback preserves coarse class cues while producing entangled objects; label-guided retraining loses most class semantics. (f) CycleGAN (non-ergodic): trajectories settle into distinct attractor basins between the two domains. Random examples from the same class are shown for each scenario.

Empirically, we observe five of the eight possible dimensional patterns across our iteration experiments, see Table 2. These patterns are not tied to a single feedback regime: different scenarios can express the same pattern, and a given scenario can transition between patterns over time. First, distinct Markov Chains can show the same local–global geometry with opposite locality: both LF-MNIST and LGR-ImageNet-5 exhibit decreasing PR_G and m_{LB} , but σ_{intra} rises in LF-MNIST (oblate expansion, OE) and falls in LGR-ImageNet-5 (coherent contraction, CC), revealing expansion vs. contraction regimes. Second, similar Markov Chains can diverge by dataset: LF-MNIST follows OE, whereas LF-ImageNet-5 follows wrinkled expansion (WE). Third, a single chain can have multiple patterns over generations: LGR-MNIST begins in CC and later shifts to wrinkled contraction (WC; m_{LB} turns upward). By contrast, CycleGAN is non-ergodic: trajectories do not settle into a single invariant subspace but switch among multiple modes (see Fig.2-f), with significant step-to-step fluctuations in PR_G , m_{LB} , and σ_{intra} ; the overall trend follows coherent expansion (CE), but it does not exhibit neural resonance.

3.2 Data Compressibility

We find that generational dynamics are sensitive to data compressibility. On MNIST, a highly compressible dataset, label-guided and unconditional retraining quickly contract the latent manifold yet retain task-relevant semantics, see

Fig. 2(b–c). The outcome is increasing repetitiveness rather than outright semantic failure. In the latent-feedback setting on MNIST (Fig. 2-a), semantics persist even longer: the chain drifts slowly toward collapse, with fine details gradually eroding while digits remain recognizable over many generations. By contrast, on a diversity-demanding dataset (ImageNet-5), semantic coherence collapses rapidly: within five feedback rounds the samples lose most object semantics, and the chain converges to low-entropy textures or generic color blobs despite identical sampling budgets and optimization settings (Fig. 2-e).

Taken together, these results demonstrate that collapse is not an artifact of a particular feedback regime: across regimes, compressibility primarily governs the timeline and the failure mode: highly compressible data drift into repetition, whereas diversity-demanding data undergo early semantic erosion.

4 Discussion

We have shown that iterative generative feedback creates a unifying behavior, *neural resonance*, in which representations converge to a low-dimensional invariant manifold when (and only when) directional contraction and ergodicity are both present. The resulting dynamics exhibit a transient-to-stationary progression that we diagnose in practice with complementary drift measures (local and cumulative FID). To interpret how manifold geometry evolve, we introduced a compact eight-pattern taxonomy linking local and global dimensional behavior; across regimes we observe five of these patterns. We also discuss non-ergodic feedback systems that switch among multiple modes rather than settling into a single invariant subspace, and therefore do not exhibit neural resonance. Data compressibility emerges as an important driver of outcomes: highly compressible data drift toward repetition while retaining semantics longer, whereas diversity-demanding data undergo early semantic erosion. Taken together, these risks create a practical asymmetry: models trained early on cleaner corpora/datasets enjoy a first-mover advantage, whereas downstream learners trained on synthetic-heavy mixtures face distribution shift, loss of rare concepts, and accelerated degeneration.

5 Methods

We study five iterative-feedback scenarios: (i) a functional analogue of Lucier’s feedback loop, implemented by repeatedly filtering audio through measured impulse responses of physical spaces [6]; (ii) CycleGAN, where pre-trained image-to-image translators are reapplied in a loop across domains [7]; and three diffusion-based settings on MNIST and ImageNet-5—(iii) latent-feedback, where diffusion model is conditioned on latent image representations, (iv) label-guided retrained, where diffusion model is conditioned on class-labels, and (v) unconditional retrained models, where no conditional information is used. In all cases, we view one application of the operator as a ‘generation’ and compose it over $n=0, \dots, N$.

First two experiments, Lucier’s functional analogue and CycleGAN serve as non-ergodic chains, and the rest three experiments are ergodic chains. The *unconditional retrained* model uses no conditioning and is trained *from scratch* at each generation on samples produced by the previous generation. The *label-guided retrained* model conditions on class labels via the standard conditional-diffusion interface and is likewise retrained from scratch each generation on the newly generated dataset. The *latent-feedback* model is trained *once* on the original dataset and then held fixed; conditioning is provided by n -dimensional feature vectors extracted from a classifier (locally trained for MNIST; Inception-V3 for ImageNet-5). Only the conditioning inputs—i.e., the images used to compute features—participate in the feedback loop, while the diffusion backbone remains unchanged. This design isolates the role of conditioning: retrained models evolve parameters across generations, whereas latent-feedback applies a fixed generator driven by iteratively updated conditioning signals. All diffusion-based experiments operate under matched sample budgets and sampler schedules.

5.1 Lucier’s Feedback Experiment

We do not physically reproduce Lucier’s sonic art piece; instead, following Abel et al. [6], we implement a *functional analogue* of the process as a time-homogeneous Markov operator. Specifically, let h denote an acoustic impulse response (IR) of a physical space and x an audio signal. One generation applies the linear time-invariant mapping

$$X_{n+1} = T_h(X_n) = \text{norm}(X_n * h), \quad (1)$$

where $*$ denotes convolution and $\text{norm}(\cdot)$ rescales the output to a fixed reference level to avoid trivial decay or blow-up. This induces a deterministic, time-homogeneous kernel $K(X, \cdot) = \delta_{T_h(X)}$; because no stochasticity is injected, the chain lacks one-step positive density and serves as a non-ergodic comparator in our study.

To instantiate T_h , we selected IRs from *ten* distinct physical spaces in the OpenAIR corpus [8] and iteratively filtered a continuous reading of *War and Peace* (Leo Tolstoy) for $N=50$ generations per IR. Audio was converted to mono,

amplitude-normalized, and convolved with each IR (FFT-based implementation); outputs were re-normalized at every generation and fed back as inputs to the next. We emphasize that this is *not* Lucier’s room–record/replay loop, but a fixed-operator analogue that captures the same feedback motif. Consistent with its non-ergodic nature, this system does not exhibit neural resonance in our sense: trajectories approach absorptive attractors determined by the filter, rather than a unique, noise-smoothed stationary distribution.

5.2 CycleGAN Experiment

For image-to-image translation we use a pre-trained CycleGAN [7] as operator T in an iterative loop. CycleGAN comprises two generators, $F_{A \rightarrow B}$ and $F_{B \rightarrow A}$, that map between domains A and B (here, *Horse* and *Zebra*). Starting from each domain separately, we define a time-homogeneous update by composing the translators:

$$X_{n+1}^{(A)} = F_{B \rightarrow A}(F_{A \rightarrow B}(X_n^{(A)})), \quad X_{n+1}^{(B)} = F_{A \rightarrow B}(F_{B \rightarrow A}(X_n^{(B)})), \quad (2)$$

and iterate for $N=200$ generations in each direction (*Horse*→*Zebra*→*Horse* and *Zebra*→*Horse*→*Zebra*). Inputs are drawn from the standard *Horse*↔*Zebra* dataset; images are resized to the model’s native resolution and intensity-scaled to the network’s input range before each application. With weights fixed and no stochasticity injected, this induces a deterministic, time-homogeneous Markov kernel that lacks one-step positive density and is therefore non-ergodic.

Empirically, the loop does not exhibit neural resonance: trajectories tend to settle into attractor basins (texture/stripe templates) that depend on the starting image and domain, yielding apparent drift plateaus that reflect absorption (as described in Shumailov et al. [2]) rather than convergence to a unique, noise-smoothed stationary distribution. Full manifold-geometry curves are reported in the Supplementary Materials.

5.3 MNIST Experiments

All MNIST experiments (latent–feedback, label–guided retrained, unconditional retrained) use the *same* diffusion backbone and training recipe, following Dhariwal and Nichol’s U-Net design [9]. We employ a 64–channel U-Net with self–attention at 14×14 and 7×7 spatial resolutions, trained for 200,000 optimizer steps with batch size 256 using Adam. Unless otherwise noted, we use 1,000 diffusion steps with a linear noise schedule and the same sampler schedule across scenarios. The image resolution is MNIST native (28×28 , single channel); all other hyperparameters are matched across scenarios (full details in Code).

Retrained diffusion, label–guided and unconditional: For the *unconditional retrained* model, no conditioning is used. For the *label–guided retrained* model, class labels provide conditioning via the standard conditional–diffusion interface. In both cases, at generation n we train a fresh model θ_{n+1} from scratch solely on the synthetic dataset produced by the previous generation, D_n , for a total of $N=100$ iterations; no real data are mixed in subsequent generations. Each generation we sample 5,000 images per class (50,000 total) to form D_{n+1} , which then becomes the training set for subsequent generation. Sampler steps, schedules, and seeds are held fixed across generations.

Latent–feedback diffusion: For the *latent–feedback* model, a single conditional diffusion model θ_0 is trained once on the MNIST training set and then *frozen*. Conditioning signals are n –dimensional feature vectors extracted from a pre–trained MNIST classifier, specifically from a high-level convolutional layer before global pooling. Let $f(\cdot)$ denote this feature map. At generation n , given conditioning images $\{x_n^{(i)}\}$, we compute $c_n^{(i)} = f(x_n^{(i)})$ and generate $x_{n+1}^{(i)} \sim p_\theta(\cdot | c_n^{(i)})$, producing one image per conditioning vector. The first generation uses the 10,000 MNIST *test* images as conditioning inputs (yielding 10,000 generated images); thereafter, only the *conditioning images* participate in the feedback loop for next 250 iterations: the synthetic set from generation $n+1$ becomes the conditioning set for generation $n+2$, while the diffusion backbone and all sampling hyperparameters remain unchanged. This design isolates feedback to the conditioning stream, in contrast to the parameter–evolving retraining setups. Additional training and sampling details, including exact feature dimensionality and classifier architecture, are provided with the code.

5.4 ImageNet-5 Experiments

Both ImageNet-5 experiments—latent–feedback and label–guided retrained diffusion—use the *same* backbone and training recipe, following the U-Net design of Dhariwal and Nichol [9]. We employ a 128–channel U-Net with self–attention at spatial resolutions 32×32 , 16×16 , and 8×8 , trained for 300,000 optimizer steps with batch size 40 using Adam. Unless noted, we use 1,000 diffusion steps with a linear noise schedule and identical sampler settings across scenarios. Images are processed at $128 \times 128 \times 3$ with standard normalization. Hyperparameters, augmentation, and optimizer details are matched across scenarios.

Label–guided retrained diffusion: The *label–guided retrained* model conditions on class labels via the standard conditional–diffusion interface and follows an *evolving–operator* protocol: at generation n , a fresh model θ_{n+1} is

trained *from scratch* solely on the synthetic dataset produced by the previous generation, D_n . Each generation we sample 50,000 images (5,000 per class) to form D_{n+1} , which becomes the training set for subsequent generation ($N=10$). No real images are mixed after $n=0$. Sampler schedules, diffusion steps, and seeds are held fixed across generations.

Latent-feedback diffusion: The *latent-feedback* model is trained *once* on 50,000 ImageNet-5 training images and then frozen; feedback acts only through the conditioning stream. Conditioning vectors are extracted with a pre-trained Inception-V3: for an image x , we compute a high-level feature $c=f(x)$. For sampling at generation $n=0$, we randomly select 10,000 images (2,000 per class) to form the conditioning set $\{c_0^{(i)}=f(x^i)\}$ and generate one sample per conditioning vector. Thereafter, the *synthetic* images from generation n are fed back to the feature extractor to produce conditioning vector for generation $n+1$ and so on for $N=50$, while the diffusion backbone θ_0 and all sampling hyperparameters remain unchanged.

A Related Work

Recent investigations into iterative feedback loops focus primarily on two domains: *language models* and *image-generative models*. In both areas, researchers explore two training protocols—fine-tuning and full-retraining. *Fine-tuning* studies start with a pretrained network and repeatedly train on its own synthetic outputs, typically uncovering semantic drift or diversity loss. By contrast, *full-retraining* approaches initialize fresh models from scratch at every generation and optimize them using previous generation’s data. In this section, we revisit both model types.

A.1 Language Models

Shumailov et al. [2] find model collapse in fine-tuned large-scale language models (LLMs) in a fully-synthetic iterative feedback loop. An iterative feedback loop arises when successive generations of generative models are trained (or fine-tuned) on data produced by their predecessors. It is called ‘fully-synthetic’ when the model is trained only with the generated data. They formally define collapse as the progressive loss of low-probability (tail) events, ultimately converging to a narrow, low-variance distribution. The paper traces the root causes to (i) *statistical-approximation error*—finite sampling inevitably drops rare events, (ii) *functional-approximation error* from limitations of the learning procedure, and (iii) *functional expressivity error* from imperfect model capacity. Together these errors accumulate, causing the distribution to drift progressively away from the true one. The authors conclude that even tiny proportions of synthetic data, if recursively reused without continual infusion of fresh real samples, leads to irreversible forgetting. The authors call for watermarking, provenance tracking, and systematic infusion of real data to preserve model quality.

Extending these findings, Dohmatob et al. [10] re-examine this phenomenon in a simplified setting of kernel regression. They show how adding synthetic data changes scaling laws and they propose adaptive regularization that partially mitigates collapse. They provide a theoretical framework of model collapse through the lens of scaling laws and propose an adaptive regularization technique to at least partially mitigate model collapse.

Guo et al. [11] probe the language richness of LLMs under iterative fine-tuning on their own outputs. They introduce a three-tier evaluation suite that measures lexical, syntactic, and semantic diversities. Across all metrics, linguistic variety declines monotonically across fine-tuning cycles: vocabulary shrinks, syntactic constructions homogenize, and Sentence-BERT embeddings cluster more tightly. They conclude that synthetic-only fine-tuning poses a systemic risk of linguistic flattening even when overall performance looks healthy, and they recommend diversity-aware objectives and routine mixing of fresh human data to avoid long-term erosion of language richness.

Briesch et al. [12] present a study of iterative feedback loops in language models trained from scratch. They experiment with a logic-expression dataset—where correctness can be unambiguously evaluated—to measure both accuracy and diversity across generations. They find that while syntactic and semantic correctness of generated expressions initially improves over early generations, lexical diversity monotonically declines, collapsing toward nearly zero diversity within 50 full-synthetic generations. They further show that incremental or expanding data cycles—where a fraction of real data is retained or added each round—can slow but not prevent diversity loss.

A.2 Image Generative Models

Model collapse in image synthesis models was investigated by Shumailov et al. [2], who demonstrated—with a VAE trained on MNIST—that repeatedly fine-tuning a model on its own samples drives the latent manifold toward degeneration. In their experiment, each generation draws fresh latent codes from a Gaussian prior, decodes them into images, and then treats these outputs as the sole training data for the next iteration. After only a handful of iterations, the VAE’s representations collapse toward the latent mean: classes blur and become indistinguishable, and the encoder assigns high confidence to increasingly featureless digits—marking a collapse of both diversity and semantics. Since this seminal result, researchers have studied model collapse under different architectures and training schemes [13–19], while theoretical work probes its statistical and dynamical underpinnings, proposing formal criteria and mitigation strategies [20–22].

Alemohammad et al. [13] coin the term *Model Autophagy Disorder* (MAD) to describe this collapse by analogy to mad cow disease. They analyze three feedback regimes: (i) a *fully-synthetic* loop, where each new model is trained only on data from its predecessor; (ii) a *synthetic-augmentation* loop, which retains a fixed cache of real images in each round; and (iii) a *fresh-data* loop, which injects new real samples in every generation. Across multiple models and different datasets, they show that without sufficient fresh data injection in every generation, visual quality (precision) or diversity (recall) collapse within only a few iterations. They conclude that any self-consuming pipeline lacking fresh data ultimately collapses, progressively amplifying artifacts or shrinking support. Gerstgrasser et al. [14] arrive at a similar conclusion from an error analysis perspective. They find that replacing the real corpus with model outputs drives test loss upward. By contrast, concatenating each synthetic batch with the existing real-plus-synthetic pool keeps error stable

and preserves both quality and diversity, without requiring special regularizers or temperature-sampling tricks. Bertrand et al. [17] introduce a fine-tuning framework based on mixed dataset—composed of real and synthetic images—and show that the long-term fate of an iterative feedback loop depends on one scalar: the per-round real-to-synthetic ratio λ . They also highlight that the critical λ -threshold is architecture- and resolution-dependent. Together, they establish that a competent seed model along with enough real data per round can stabilize model collapse, but removing real images drives the process toward degeneration.

Hataya et al. [15] use large scale datasets like ImageNet and COCO with diffusion models to study the impact of generation collapse on future datasets and model performance. They replace varying proportions of real ImageNet or COCO images with generated fakes to mimic future web contamination. On the ImageNet classification task, ResNet-50, Swin-S and ConvNeXt-T suffer only minor top-1 drops up to 40% synthetic data, but accuracy plummets by 10-15 percentage points at 80% and collapses to 15% when training solely on synthetic images. Experiments on a COCO captioning task show the same monotonic degradation. For image generation, an ID-DPM [9] trained on the mixes exhibits rising precision but sharply falling recall, revealing mode contraction. Similarly, Yoon et al. [18] also explore model collapse in text-to-image generative models, where a pretrained text-to-image diffusion model is repeatedly finetuned on its own synthetic outputs (without the addition of real data) using a fixed prompt set. They first conduct extensive empirical studies across four diverse datasets (Pokémon, Kumapi, Butterfly, CelebA-1k), varying common hyperparameters to find that classifier-free guidance (CFG) scale is by far the dominant factor for model collapse. Low CFG (e.g. 1.0) yields smooth but blurry low-frequency degradation, high CFG (e.g. 7.5) produces saturated, repetitive high-frequency artifacts, and an intermediate CFG (dataset-specific, around 2.5 or 1.5) best balances fidelity and stability. Inspired by genetic mutations, they propose ReDiFine (reusable diffusion fine-tuning), which combines condition-drop fine-tuning (to inject randomness) with CFG scheduling as a plug-and-play remedy. It dramatically reduces collapse rate while preserving first-iteration quality without data specific hyperparameter tuning.

Bohacek and Farid [16] demonstrate that Stable Diffusion v2.1 is highly susceptible to iterative feedback: after just five iterations of retraining on its own outputs, the generated images of human faces become severely distorted and homogeneous, even when the retraining set contains as few as 3% synthetic images mixed with 97% real data. Across mixtures from 3 to 100% synthetic images, FID rises and CLIP similarity falls sharply after a brief initial uptick, confirming rapid declines in both photorealism and semantic alignment. They also perform a healing experiment—five additional epochs on only real images—and find that it somewhat restores mean FID and most of the CLIP score, yet residual artifacts and elevated CLIP variance indicate that the damage is only partly reversible. They conclude that even minimal contamination of future datasets with model-generated content can trigger irreversible quality and diversity loss. Gillman et al. [19] address the instability and collapse by proposing a self-correction framework designed to stabilize this process. They implement scalable self-correction via expert knowledge—K-means ‘anchor’ projections for correcting MNIST-based models and a physics-simulator-based corrector for human motion models—and demonstrate on a challenging text-to-motion diffusion task that self-corrected loops avoid collapse even at 100% synthetic data, consistently outperforming uncorrected loops. Their results suggest that a reliable correction function can safeguard generative training against the degenerative effects of synthetic-only retraining.

Our work pushes the study of model collapse beyond conventional fine-tuning and full-retraining loops by dissecting three complementary feedback regimes through the lens of Markov processes. (i) In latent-feedback models, a frozen, pretrained classifier supplies n -dimensional feature vectors that serve as high-level conditioning for the generative model at every generation. (ii) Label-guided retraining forgoes pretrained features: each new generator is trained from scratch, conditioned only on class labels, allowing us to isolate the effect of coarse-grained supervision. (iii) Unconditional retraining removes all guidance, exposing the dynamics of a purely self-referential pipeline. By contrasting these settings we reveal how the type and granularity of conditioning govern the speed, form, and the inevitability of collapse under fully synthetic-data conditions. Finally, we interpret collapse through the notion of *neural resonance*, defined as the emergence of a low-dimensional invariant subspace that remains unchanged under repeated generative updates; our analysis shows that each feedback regime converges toward such a resonant subspace at a characteristic rate, providing a unifying explanation for the observed patterns of degradation.

B Datasets & Metrics

This section details the datasets employed in our experiments and outlines the evaluation metrics used to probe the Markov chains.

B.1 Datasets

We evaluate our framework on three datasets: MNIST (Modified National Institute of Standards and Technology) [23], ImageNet-5, and OpenAIR [8].

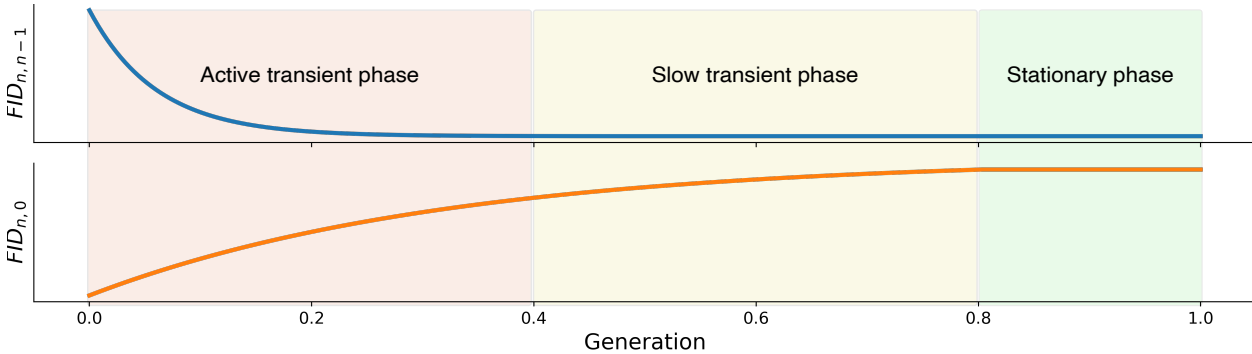


Figure 3: **A idealized example of local and cumulative drifts in generational Markov chains.** The blue curve ($FID_{n,n-1}$) shows local drift between successive generations, and the orange curve ($FID_{n,0}$) shows cumulative drift from the original data. When both curves have steep slopes, the chain is in an *active transient* phase; when one curve flattens and the other changes slowly, it is in a *slow transient* phase; and when both plateau, the system has reached empirical stationarity.

The MNIST dataset is a standard benchmark of 70,000 grayscale 28×28 images of handwritten digits (0-9). The dataset is divided into a training set of 60,000 and a test set of 10,000 images.

ImageNet-5 is a custom, five-class subset of ImageNet [24], created by leveraging its hierarchical label structure. We merged related ImageNet synsets into five coarse categories—Cat, Terrier Dog, Insects, Monkey, and Wading-bird, each containing $\sim 10,000$ color (RGB) images of resolution 128×128 pixels. The exact synset mappings needed to reproduce this subset are included with our code.

To emulate Lucier’s feedback loop, we convolved a continuous narration of *War & Peace* [25] with room-impulse responses from ten acoustically distinct spaces selected from the OpenAIR corpus [8]. Each impulse response defines a distinct class, yielding ten sound categories. The full list of rooms and their corresponding impulse-response files are distributed with our code.

B.2 Quantitative Metrics

We quantify the empirical behavior of each Markov chain using the *Fréchet Inception Distance* (FID). The distance from one iteration (or generation) to the next measures *local drift*, whereas distance from the original generation to a later generation measures *cumulative drift* from the data manifold; the joint trajectory of these two curves provide evidence of empirical stationarity and the onset of neural resonance. To probe the accompanying changes in latent geometry we employ three complementary statistics: (i) the within-class spread σ_{intra} , which measures class-specific spread; (ii) the Levina–Bickel intrinsic dimensionality estimate m_{LB} [5], a proxy for local degrees of freedom; and (iii) the global participation ratio PR_G , which reflects the effective dimension of the entire feature cloud. We now explain these metrics in detail.

B.2.1 Fréchet Inception Distance (FID)

FID is the 2-Wasserstein distance between two Gaussians fitted to embedded features of two sample sets S_r (real) and S_g (generated),

$$FID = \|\mu_r - \mu_g\|^2 + Tr \left(\Sigma_r + \Sigma_g - 2(\Sigma_r \Sigma_g)^{1/2} \right), \tag{3}$$

where μ_r, Σ_r and μ_g, Σ_g are the mean vectors and covariance matrices of the real and generated distributions, respectively. The embeddings are extracted from a pre-trained network (usually Inception-V3 [26] or a locally trained classification network). Lower values indicate closer agreement between real and generated distributions in latent space.

In our experiments, we compute FID scores across distributions generated at successive iterations. As an example, suppose that X_0 is the original data distribution (real images) and X_1, X_2, \dots, X_N are the generated distributions at each generation n , i.e., the output of the generative samples obtained after the n^{th} iteration. We estimate the FID score at the classification layer of Inception-V3 for ImageNet-5, and at convolution layers of pretrained networks for MNIST. We track two complementary scores (Fig. 3):

1. *Local-drift* ($FID_{n,n-1} = FID_{X_n, X_{n-1}}$) measures how much each new generation differs from the last. Smaller values indicate low drift across generations, consistent with local stationarity.

2. *Cumulative-drift* ($\text{FID}_{n,0} = \text{FID}_{X_n, X_0}$) estimates the cumulative distance traveled from the original distribution.

These two scores together provide evidence consistent with empirical stationarity. As shown in Fig. 3, if both $\text{FID}_{n,n-1}$ and $\text{FID}_{n,0}$ have large negative/positive slope, the chain is in an *active transient* phase; if one flattens while the other changes slowly, the chain is in a *slow transient* phase; if both flatten, the evidence points to empirical *stationarity*.

B.2.2 Intra-Class Spread (σ_{intra})

Intra-class root-mean square Euclidean deviation [27], or simply *intra-class spread*, measures the average local spread of latent representations within each semantic category, reflecting how spread or compact individual class clusters are. Formally, for C classes with samples $X_c \subset \mathbb{R}^D$ and centroids μ_c of latent feature x_L ,

$$\sigma_{\text{intra}} = \frac{1}{C} \sum_{c=1}^C \sqrt{\frac{1}{|X_c|} \sum_{x \in X_c} \|x - \mu_c\|^2}, \quad \text{where } \mu_c = \frac{1}{|X_c|} \sum_{x \in X_c} x_L. \quad (4)$$

Here, the term under the square-root is the mean-squared deviation of class- c points from their centroid, and averaging over classes yields a single statistic capturing the typical cluster radius. σ_{intra} provides a robust measure of local cluster behavior within each category, offering a gauge of how iterative processing reshapes class-specific features over time.

Behavior of σ_{intra} : It offers a granular view of how neural resonance reshapes the manifold in the vicinity of each data point. An increase in σ_{intra} indicates *local semantic expansion*, where cluster points diverge along latent axes across generations. A decrease indicates *semantic contraction*, where clusters tighten over generations.

B.2.3 Intrinsic Dimensionality (m_{LB})

Intrinsic dimensionality (Levina–Bickel Estimator [5]) captures the number of ‘free’ directions in which data locally vary, i.e., the dimensionality of the manifold on which the high-dimensional points really lie. In a smooth latent manifold, each point x_i lives in a tiny patch that is well-approximated by an m -dimensional Euclidean neighborhood, so that the number of nearby samples within radius r scales like r^m ($\text{Volume}_m(r) \propto r^m$). The expected number of points within radius r is proportional to r^m ; Levina and Bickel’s method harnesses this scaling law by examining the ratios of the k -th nearest-neighbor distance $T_i(k)$ to the distances $T_i(j)$ of the first $k-1$ neighbors,

$$m_{\text{LB}} = \frac{1}{n} \sum_{i=1}^n \hat{m}_i, \quad \text{where } \hat{m}_i = \left[\frac{1}{k-1} \sum_{j=1}^{k-1} \ln \frac{T_i(k)}{T_i(j)} \right]^{-1}. \quad (5)$$

Here n is the number of samples, \hat{m}_i is the estimated dimension around point i , and k is the neighbor count. Averaging over all observations n of a data cluster provides an estimate of local dimensionality. Though sensitive to number of neighbors k , the intrinsic dimensionality quantifies the manifold’s *effective* number of independent axes: it is the local ‘degrees of freedom’ available for data variation, and averaging \hat{m}_i (Eq. 5) over all points delivers a robust measure of the local latent representation’s geometric complexity.

Intrinsic dimensionality is sensitive to folds—here termed ‘*wrinkles*’—in the latent manifold. A *wrinkle* is a localized, low-amplitude perturbation that introduces subtle new axes of variation within a small neighborhood, thereby raising local dimensionality without substantially altering the global structure. Geometrically, this represents small-scale deviations from the manifold’s smooth, low-curvature core—localized folds or nonlinearities that increase dimensionality in a restricted neighborhood. Rather than altering the manifold’s broad, global shape, wrinkles inject fine-grained ripples that raise its local dimensionality without changing its overall coarse geometry.

Behavior of m_{LB} : A decline in intrinsic dimensionality denotes semantic contraction, reflecting the manifold’s collapse onto a diminishing set of principal axes. In contrast, an increase in intrinsic dimensionality signals either genuine expansion into previously unoccupied subspaces or the emergence of localized ‘wrinkles’ that transiently elevate neighborhood-level degrees of freedom even amid local semantic contraction.

B.2.4 Participation Ratio (PR)

The participation ratio quantifies the *effective* number of principal axes that capture latent variance, serving as an alternate measure of manifold dimensionality [28, 29]. Given the eigenvalues $\{\lambda_i\}_{i=1}^D$ of the empirical covariance matrix of the latent features, participation ratio is,

$$\text{PR} = \frac{(\sum_{i=1}^D \lambda_i)^2}{\sum_{i=1}^D \lambda_i^2}. \quad (6)$$

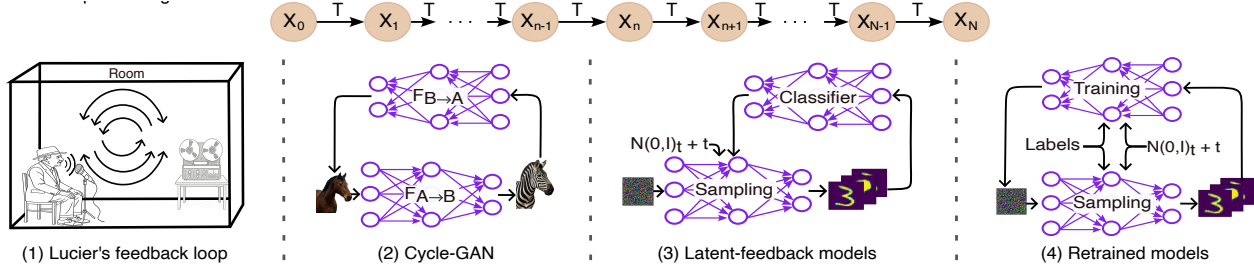


Figure 4: **A high-level representation of the Iterative feedback process.** X_n represents the current distribution of images at generation n and $T(\cdot)$ is the transformation operator. The framework unifies five feedback settings—Lucier’s acoustic experiment, cyclic image translation (CycleGAN), latent-feedback diffusion, and two retrained diffusion models (label-guided and unconditional)—each representing a distinct form of iterative feedback. Together they illustrate how successive generations of models form a Markov process and their shared dynamics.

Here D is the total number of eigenvalues, typically $D=n$. If variance is concentrated in a single direction, $PR = 1$; if it is evenly distributed across k orthogonal directions, $PR = k$.

The participation ratio can be estimated at different levels for an image distribution—either at the class level, considering samples within each category, or at the global level, considering the entire distribution. In this work, we compute global participation ratio (PR_G) from the full eigen-spectrum of latent features computed across the entire dataset. PR_G is a hyperparameter-free, robust estimate of the manifold’s global ‘degrees of freedom’.

Behavior of PR_G :

An increase in PR_G denotes *global expansion*, implying that variance has become more uniformly spread across a larger number of principal axes. Conversely, a decrease in PR_G signals *global contraction*, as the latent representation progressively collapses onto a smaller subset of dominant directions. Participation ratio remains effectively invariant under small-magnitude ‘wrinkles,’ changing only when local perturbations inject enough variance into new directions to alter the global covariance spectrum.

Relationship between PR_G and m_{LB} : Although both metrics quantify dimensionality of a latent space, they capture complementary aspects of latent-space geometry. PR_G is derived from the full eigen-spectrum of the covariance matrix and therefore reflects the *global* distribution of second-moment variance: if most variance is concentrated along only a few axes, PR_G will be small even when the manifold locally meanders through many minor directions. By contrast, m_{LB} is a maximum likelihood estimation based on how neighbor distances scale with radius and is thus sensitive to fine-scale curvature or wrinkles that may add local directions without materially affecting PR_G .

The two metrics coincide on linear or nearly linear subspaces with uniformly distributed samples—such as a well-spread Gaussian blob—because under those conditions local scaling and global second moments capture the same structure, rising or falling together. They diverge, however, on strongly nonlinear manifolds. In short, PR_G answers “how many axes carry most of the variance for the whole distribution?” whereas m_{LB} asks “how many directions does the manifold reveal locally?” Used together, the two measures provide a fuller picture of latent-space structure than either can supply alone.

C Generative Feedback as a Markov Chain: Expanded

We begin with an initial distribution of images (X_0). Repeated application of a transformation operator T yields successive distributions $\{X_0, X_1, X_2, \dots\}$, where each generation depends only on its predecessor. This naturally defines a Markov chain across iterative generations.

We refer to this process as a *generational Markov chain* (GMC). Its characteristics are determined entirely by the properties of the operator T . If T injects randomness, the chain explores broadly before settling into a stationary distribution; if T is deterministic or lacks randomness, the chain instead converges to a fixed point or local attractor. In this section, we present a detailed analysis of different iterative feedback frameworks shown in Fig. 4 and explore their characteristics as a GMC.

Formally, let X_0 denote the initial distribution—an audio waveform in Lucier’s feedback loop or an image distribution in generative models. The operator T acts iteratively on this domain, mapping $T: \mathcal{X} \rightarrow \mathcal{X}$, where,

$$\mathcal{X} = \begin{cases} \mathbb{R}^d & \text{Lucier’s Feedback} \\ \mathbb{R}^{H \times W \times C}, & \text{CycleGAN} \\ \mathbb{R}^{H \times W \times C}, & \text{Latent-Feedback} \\ \{x \sim p_{\text{data}}(x) \mid x \in \mathbb{R}^{H \times W \times C}\}, & \text{Uncond-Retrained} \\ \{(x, y) \sim p_{\text{data}}(x, y) \mid x \in \mathbb{R}^{H \times W \times C}, y \in \{1, \dots, K\}\}. & \text{Cond-Retrained} \end{cases}$$

In this context, $\mathbb{R}^{H \times W \times C}$ represents the space of images with spatial dimensions $H \times W$ and C color channels. Here, $x \in \mathbb{R}^{H \times W \times C}$ denotes a single image sample. and y represents its associated class label with K distinct classes. The distribution $p_{\text{data}}(\cdot)$ characterizes the empirical probability distribution of the dataset. For each iterative step $X_{n+1} = T(X_n)$, operator T is

$$T = \begin{cases} h * (\cdot), & \text{Lucier’s Feedback Loop} \\ F_{A \rightarrow B}(F_{B \rightarrow A}(\cdot)), & \text{CycleGAN} \\ D(\cdot \mid f(\cdot)), & \text{Latent-Feedback Models} \\ \text{Sample}(\text{Train}(\cdot)), & \text{Un/Conditional Retrained Models} \end{cases} \quad (7)$$

where h denotes a convolutional kernel applied iteratively in the acoustic feedback scenario [6]; $F_{A \rightarrow B}(F_{B \rightarrow A}(\cdot))$ constitutes a cyclic operator implemented via paired generative adversarial networks (GAN) over two domains A and B , $F_{A \rightarrow B}$ and $F_{B \rightarrow A}$; $D(\cdot \mid f(\cdot))$ symbolizes latent-feedback sampling with a pre-trained generative diffusion model D guided by features extracted from a pre-trained classification network $f(\cdot)$; and finally, $\text{Sample}(\text{Train}(\cdot))$ describes an iterative process of repeated model retraining and subsequent DDPM (denoising diffusion probabilistic models) sampling [30]. This framework captures the common mechanism that underlies diverse collapse scenarios—including the ‘model collapse’ phenomenon [2], which we refer to as *generational collapse*—and, under the conditions detailed in Section D, unifies them within the concept of *neural resonance*.

Generational collapse occurs when repeated application of a transformation operator amplifies structural or semantic preferences. At the same time, it suppresses semantic variance in the generated distribution. Whether arising from architectural or model biases, or from retraining-induced biases, each iteration pushes the generated distribution of GMCs closer to a low-dimensional attractor state by altering the effective feature support of the output distribution in latent space. Ultimately, the GMCs converge on this attractor state, producing distributions that remain unchanged under further iterations.

C.1 Proof of Markov Property

We model this iterative framework as a Markov process over generations. Figure 4 illustrates a generational Markov chain, where the repeated application of the operator $T(\cdot)$ yields $X_{n+1} = T(X_n)$. The diagram depicts this progression: from the initial distribution X_0 through successive generations X_1, X_2, \dots , ultimately approaching a stationary distribution X_N .

All four experimental settings—functional analogue of Lucier’s feedback loop, CycleGAN translation, latent-feedback diffusion, and retrained diffusion—fit this framework as iterative operators acting on a state space \mathbb{E} . We analyze the *Markovian* nature of the iterative framework, i.e., a process in which the next state depends only on the present state, not the full history. Formally, a Markov chain is a stochastic process $\{X_n\}$ that satisfies the property:

$$P(X_{n+1} \mid X_n, X_{n-1}, \dots, X_0) = P(X_{n+1} \mid X_n). \quad (8)$$

Lucier’s feedback loop: For the functional analogue of Lucier’s feedback loop, let the audio waveform at iteration n be X_n . The update is

$$X_{n+1} = T(X_n) \Rightarrow X_{n+1} = h * (X_n), \quad (9)$$

where h is a fixed convolution kernel and $*$ denotes the one-dimensional convolution operation. Since $T(\cdot)$ is fixed, the Markov property holds directly.

CycleGAN: For CycleGAN, an image at generation n is mapped as

$$X_{n+1} = T(X_n) \Rightarrow X_{n+1} = F_{A \rightarrow B}(F_{B \rightarrow A}(X_n)), \quad (10)$$

where $F_{A \rightarrow B}: A \rightarrow B$ and $F_{B \rightarrow A}: B \rightarrow A$ are fixed neural network mappings and X_n is an image sample. Since the operator is deterministic, the Markov property is satisfied.

Latent-feedback models: For latent-feedback diffusion, each iteration samples from a fixed diffusion model \mathcal{D} , conditioned on features from a deterministic extractor $f(\cdot)$:

$$X_{n+1} = T(X_n) \Rightarrow X_{n+1} = \mathcal{D}(\cdot | f(X_n)), \quad (11)$$

where, X_n is a distribution. Because each step depends only on the previous latent state, the process is Markovian.

Retrained diffusion models:

In retrained diffusion models, each new distribution X_{n+1} depends not only on X_n but also on the model parameters \mathcal{D}_{n+1} . Thus, at the distribution level, the Markov property does not hold. However, if we expand the state to include both the parameters and samples— (\mathcal{D}_n, X_n) —the chain becomes Markovian:

$$P((\mathcal{D}_{n+1}, X_{n+1}) | (\mathcal{D}_n, X_n), \dots) = P((\mathcal{D}_{n+1}, X_{n+1}) | (\mathcal{D}_n, X_n)). \quad (12)$$

Hence retrained models admit a Markovian representation in the joint parameter-sample space. The operator T can be applied at a sample level or at distribution level; for simplicity, we treat X_n as a distribution hereafter.

C.2 Ergodicity of GMCs: Sketch Proof

Before giving the full technical proof in §3.3, we sketch the main ideas behind the ergodic behavior of generational Markov chains. In what follows, X_n is considered as a distribution, unless stated otherwise. We provide the sketch proof and the expander proof in §3.3 for diffusion-based GMCs, but it can be extended to other GMCs with different state space.

Setup: The state of the GMC at generation n is a distribution X_n over the pixel cube $\mathbf{E} = [0, 1]^{H \times W \times C}$, that is, all images of shape $H \times W \times C$ with pixel values in $[0, 1]$. A single generational update is implemented by running reverse-DDPM sampling procedure (Alg. 1) conditioned on features $f(X_n)$: starting from Gaussian noise, the sampler repeatedly, adds Gaussian noise (with full support), and applies a smooth neural network update that nudges the sample toward high-density regions, and finally returns new images $x_i \in X_{n+1}$ in \mathbf{E} [30]. This defines a Markov chain $X_{n+1} = T(X_n)$, where T is the one-generation transition rule. We claim that the diffusion-based generational chains are ergodic: in the long run it forgets its starting point and converges to a unique long-run distribution over images. We define this property in terms of continuous state space Markov chains.

The argument relies on three intuitive properties of the dynamics of reverse-diffusion: (i) *Everywhere-noisy transitions*, In Alg. 1, at each reverse step, we inject Gaussian noise whose density is strictly positive everywhere in \mathbf{E} . No region is ever assigned zero probability by the noise alone. (ii) *Smooth neural updates*, the neural network in the sampler is built from dot products and standard activations (ReLU, sigmoid, tanh), so small changes in its input produce small changes in its output almost everywhere. The overall DDPM update is a smooth deformation of the injected noise. Finally, (iii) *Bounded image space*, all generations are kept inside a fixed bounded region: pixel values are clipped into $[0, 1]$, so the chain moves within a compact set of possible images and cannot escape to infinity. For a continuous state-space Markov chain, ergodicity requires showing three properties: irreducibility, aperiodicity, and repeated mixing in a bounded space. We can use the intuitive properties of reverse-diffusion to prove that the generational Markov chain has these properties.

Irreducibility: A Markov chain is irreducible if a distribution over a given state space assigns nonzero probability mass across the entire state space in the limit. Consider one full generational update, from X_n to X_{n+1} . We first sample a Gaussian noise vector with nonzero probability everywhere, then pass it through a smooth neural network plus clipping to $[0, 1]$. Because the noise covers the full space and the network does not collapse everything to a lower-dimensional set, the resulting probability distribution of X_{n+1} assigns *nonzero* probability to every region of the image cube \mathbf{E} . Intuitively, there is always some (possibly very small) chance of moving from any given image into any non-negligible region of the image space in a single transition step. This is the Markov-chain notion of being able to “eventually reach everywhere” from anywhere, and is the intuition behind irreducibility. For more details please see Sec. C.3.1.

Aperiodicity: A Markov chain is aperiodic if it does not return to a region within the state space at a regular interval (e.g., only return to a state or region after exactly 3, 6, 9, ... generations). Because the transition from X_n to X_{n+1} is noisy and smooth, the chain can not only move far away but also move around locally. Starting from a given state X_n , there is a strictly positive probability that the next state stays within a tiny neighborhood of X_n . If the chain was periodic, such local randomness would be impossible: there would be generations where it *must* move elsewhere. The presence of noise at every step breaks such rigid rhythms. This rules out fixed periods and gives the intuition for aperiodicity.

Repeated mixing in a bounded space: The chain evolves in a bounded image cube and every one-step transition has a small but strictly positive probability of landing in any given region of that cube. In other words, each generation performs a random, noisy ‘mixing move’ that never completely ignores any subset of images. Mixing leads to a strong notion of recurrence: the chain keeps coming back to every region with positive probability.

Algorithm 1 DDPM Sampling Process (reprinted from Ho et al. [30])

```

1:  $\mathbf{x}_T \sim \mathcal{N}(0, I)$ 
2: for  $t = T, \dots, 1$  do
3:    $\mathbf{z} \sim \mathcal{N}(0, I)$  if  $t > 1$  else  $\mathbf{z} = 0$  ▷ : Sample Gaussian noise
4:    $\mathbf{x}_{t-1} = \frac{1}{\sqrt{\alpha_t}} \left( \mathbf{x}_t - \frac{1 - \alpha_t}{\sqrt{1 - \alpha_t}} \varepsilon_\theta(\mathbf{x}_t, t) \right) + \sigma_t \mathbf{z}$  ▷ : Annealed Gaussian step
5: end for
6: return  $\mathbf{x}_0$ 

```

A Markov chain with these properties (irreducibility, aperiodicity, and strong mixing in a bounded state space) behaves like a well-mixed random walk. The next sections formalize this sketch in the language of continuous state-space Markov chains and provide a full measure-theoretic proof.

C.3 Ergodicity of GMCs: Expanded Proof

We illustrate the characteristics of GMCs using the latent-feedback diffusion model, though the results extend to all GMCs within our framework. The GMC operates in the state space $\mathbf{E} = [0, 1]^{H \times W \times C}$ endowed with Borel σ -field, meaning random variable x_n takes values in \mathbf{E} and are measurable with respect to that σ -field and the associated transition kernel $K(x, \cdot)$ induced by T . The transition kernel assigns a probability measure on $(\mathbf{E}, \mathcal{B}(\mathbf{E}))$ for each state x , enabling us to perform integration, and to define expectations for the process. We adopt the Lebesgue¹ measure on the bounded cube $[0, 1]^{H \times W \times C}$ as the reference measure, ensuring σ -finiteness. This implies that every one-step law $K(x, \cdot)$ —the probability distribution of the next state given the current state, of the Markov chain is continuous with respect to the measure ψ and allow us to write each transition probability in density ($k(x, y)$) form,

$$K(x, A) = \int_A k(x, y) \psi(dy), \quad x \in \mathbf{E}, A \subseteq \mathbf{E}, \quad (13)$$

where ψ never assigns a zero value to any $K(x, \cdot)$. The per-generation transition kernel, $K : \mathbf{E} \times \mathcal{B}(\mathbf{E}) \rightarrow [0, 1]$ is defined as

$$K(x, B) = \int_B P_\theta(y|f(x)) \psi(dy), \quad B \in \mathcal{B}(\mathbf{E}) \quad (14)$$

where $P_\theta(\cdot)$ is the one-step output density. Equivalently, at the level of random variables,

$$X_{n+1} \sim P_\theta(\cdot|f(X_n)), \quad n = 0, 1, \dots \quad (15)$$

and the generalized GMC is written as $\{X_n\}_{n \geq 0} : X_{n+1} \sim K(X_n, \cdot)$, where K is the transition kernel induced by T as shown in Fig. 4.

The latent-feedback generative models uses a pre-trained image classification network $f(\cdot) : \mathbf{E} \rightarrow \mathbb{R}^d$, to provide d -dimensional conditional feature vectors as conditional to the diffusion model. We follow Dhariwal and Nichol [9] for network architecture and diffusion noise schedules. We also use Langevin dynamics [31] in Denoising Diffusion Probabilistic Model (DDPM) [30] for sampling images. We briefly describe the DDPM sampling process as it is an integral part of our proof.

The DDPM sampling stage (see Alg. 1) can be viewed as a *discrete Langevin-type dynamics* run in reverse time. Starting from pure Gaussian noise $x_T \sim \mathcal{N}(0, I)$, each reverse step adds a drift term proportional to the learned score $\nabla_x \log p_\theta(x_t)$ —pulling the sample toward high-density regions—and injects *annealed* Gaussian noise (see step 4 of Alg. 1) whose variance shrinks with timestep t . The learned score field approximates the score $\nabla_x \log p_t(x_t)$ [32], while the gradually decreasing noise scale σ_t plays the role of the temperature schedule, yielding a stochastic but guided trajectory that transforms white noise into a realistic image as t marches to 0. The annealed Gaussian step guarantees a strictly positive one-step density under mild conditions.

With the above description of the generational Markov chain, we argue that the chain is ψ -irreducible, aperiodic, and positive Harris recurrent in a compact state space $\mathbf{E} = [0, 1]^{H \times W \times C}$. We base our proof on time-homogeneous kernels as required by Meyn-Tweedie theories [4] and can be extended to time-inhomogeneous kernels.

¹Lebesgue on the cube means the usual notion of volume in d -dimensions (length in 1D, area in 2D, volume in 3D, and so on), restricted to the cube $[0, 1]^{H \times W \times C}$. This provides a natural baseline measure against which probabilities and densities on the state space can be defined.

C.3.1 ψ -Irreducibility

Irreducibility means the chain is not confined: from any state, it can eventually reach every other region of the space with non-zero i.e., *everywhere noisy transition*. A Markov chain is irreducible when every state can reach every other state with positive probability in some finite number of steps i.e., the ability of a Markov chain to reach any non-null set in finite time. Formally, it is defined as:

Definition 1 (ψ -irreducible). *A kernel K is ψ -irreducible if for every $x \in \mathbf{E}$ and every measurable set A with $\psi(A) > 0$, there exists an $n \geq 1$ such that the n -step kernel $K^n(x, A) > 0$.*

Lemma C.1 (One-step positive density). *One-step diffusion-based generative Markov kernel has positive density; i.e., the one-step density $K(x, y)$ of $K(x, \cdot)$ satisfies $K(x, y) > 0$ for all $y \in \mathbf{E}$. Therefore, for any A with $\psi(A) > 0$,*

$$K(x, A) = \int_A K(x, y) \psi(dy) > 0. \quad (16)$$

Proof. Inside the one outer call to the diffusion model, we simulate DDPM sampling from i.i.d. Gaussian noise. As shown in Alg. 1, it draws $z_T \sim \mathcal{N}(0, I)$, which has positive density everywhere, followed by a smooth transport map $T_\theta^c : \mathcal{R}^{d_z} \rightarrow \mathbf{E}$ defined by the neural network.

The Gaussian has a positive density and the neural network—which, with smooth activation functions (e.g. sigmoid, tanh), defines a mapping that is continuous almost everywhere for piecewise-linear functions (e.g. ReLU)—is continuous almost everywhere, given standard neural activations (e.g., ReLU, Sigmoid, tanh). The one-step-density $K(x, y) > 0$ for all $y \in \mathbf{E}$. Therefore, Eq. 16 holds for any A with $\psi(A) > 0$. Thus, ψ -irreducibility follows directly with $n = 1$ (similar arguments are used in DDPM [30]). \square

In the proof, we make the following two assumptions which are usually satisfied in practice:

1. *Surjectivity of $f(x)$* : Even if the feature extractor maps all images in a region to the same class label—so that, from the model’s conditional prior, this region has zero density and the differences between images are invisible—the Gaussian noise injected at each sampling step has full support (positive density everywhere). This ensures that the Markov chain can still move anywhere in the state space, preserving irreducibility.
2. *Bounded outputs of neural networks*: Because T_θ^c is continuous (and often Lipschitz), small changes in the input produce only small changes in the output. This prevents the mapping from sending probability mass to pathological points like $\pm\infty$ or collapsing into Dirac spikes. As a result, the transformed density remains smooth and strictly positive.

The irreducibility proof only fails if the class-conditional sampler truly assigns zero probability to some positive-volume region of the pixel space.

C.3.2 Aperiodicity

Aperiodicity in Markov chains means the chain does not evolve in fixed cycles—returns can occur at irregular times rather than being locked to a fixed rhythm. Starting from any state, there is no fixed rhythm—such as ‘every third step’ or ‘only on even times’—that dictates when the chain can return to a set of states with positive probability. Formally, for a Markov chain with transition kernel K on a measurable state-space $(\mathbf{E}, \mathcal{B}(\mathbf{E}))$ that is ψ -irreducible for a measure ψ , the period of this chain is given as

$$d = \gcd\{n \geq 1 : K^n(x, A) > 0 \text{ for some } A \text{ with } \psi(A) > 0\} \quad (17)$$

where $K^n(x, A)$ is the probability of landing in A after exactly n -steps from x . The term ‘gcd’ is the greatest common divisor of all the step-counts and represents the period (d) of the chain. The chain becomes aperiodic if $d = 1$, i.e., if there is no clock that forces the chain to move in a fixed rhythm.

Lemma C.2 (Local self-transition). *If for every $x \in \mathbf{E}$ there exists a neighborhood $\mathcal{B}_\varepsilon(x)$ such that $K(x, \mathcal{B}_\varepsilon(x)) > 0$, the chain is aperiodic; i.e., if $\forall x \in \mathbf{E}, \exists \varepsilon > 0 : K(x, \mathcal{B}_\varepsilon(x)) > 0$, then the chain is aperiodic.*

Proof. Lemma C.1 shows that the one-step density $K(x, y)$ is strictly positive everywhere, $K(x, y) > 0, \forall x, y \in \mathbf{E}$. For any state x , a small neighborhood ball $\mathcal{B}_\varepsilon(x)$ has non-zero transition probability, ensuring aperiodicity.

$$K(x, \mathcal{B}_\varepsilon(x)) = \int_{\mathcal{B}_\varepsilon(x)} K(x, y) \psi(dy) > 0,$$

and hence, aperiodic. \square

We can also prove aperiodicity by contradiction, suppose the period $d > 1$. Then, all non-zero return probabilities would occur at step $d, 2d, 3d, \dots$. But, the Lemma C.1 says there is already a positive chance to come back in one-step, contradicting periodicity. Therefore, the chain is aperiodic with period $d = 1$. Aperiodicity leads to smooth neural updates in GMCs.

C.3.3 Harris Recurrence

In a Markov chain, Harris recurrence means that starting from any state, the chain will return to any set of states with positive measure infinitely often, with probability 1. It guarantees the chain will eventually revisit any significant portion of its state space repeatedly. We use petite-set to establish this property for generational Markov chains.

A *petite set* is a subset of the state space that, relative to the Markov kernel, ensures the chain has enough chance to mix, which is crucial for establishing ergodicity. In other words, petite sets act as ‘anchors’ where the chain does not get stuck and retains access to the rest of the space.² In our DDPM kernel, the Gaussian noise term ensures that the whole image cube is petite, even though it is uncountable. Typical images lie in the bounded pixel cube $[0, 1]^{H \times W \times C}$, and the overall state space is finite-dimensional. The reverse-DDPM transition density function is jointly continuous and strictly positive, making the entire bounded cube qualifies as a petite set. The proof proceeds as follows.

Assuming ψ -irreducibility (Lemma C.1) and aperiodicity (Lemma C.2) of our GMC with finite state space $\mathbf{E} = [0, 1]^{H \times W \times C} (\subset \mathbb{R}^{784}$ for MNIST), we apply petite set proof to prove Harris recurrence. To this end, we restate small set condition and petite set Theorems 5.5.3 from Meyn and Tweedie, 2nd edition and refer to the book for their proofs.

Lemma C.3 (Small set in finite space). *A set $C \in \mathcal{B}(\mathbf{E})$ is called a small set if there exists an $m > 0$, and a non-trivial measure v_m on $\mathcal{B}(\mathbf{E})$, such that for all $x \in C$, $B \in \mathcal{B}(\mathbf{E})$,*

$$K^m(x, B) \geq v_m(B).$$

Then, C is v_m -small.

We refer to the proof provided in Sec. 5.2, Meyn and Tweedie, 2nd edition [4].

Lemma C.4 (Petite set minorization). *A set $C \in \mathcal{B}(\mathbf{E})$ is v_a -petite if the sampled chain satisfies the bound $K_a(x, B) \geq v_a(B)$, for all $x \in C$, $B \in \mathcal{B}(\mathbf{E})$, where v_a is a non-trivial measure on $\mathcal{B}(\mathbf{E})$, stated as:*

$$\text{If } C \in \mathcal{B}(\mathbf{E}) \text{ is } v_m \text{-small, then } C \text{ is } v_{\delta_m} \text{-petite.}$$

We refer to Sec. 5.5.2 in Meyn and Tweedie (2nd edition) for its proof [4].

The reverse DDPM transition density $k(x, y)$ is jointly continuous and strictly positive on the compact set $\mathbf{E} \times \mathbf{E}$. Because $k(x, y)$ is continuous and $\mathbf{E} \times \mathbf{E}$ is compact, k cannot shrink arbitrarily close to zero without actually reaching a minimum value ε . Thus, there exists a constant $\varepsilon > 0$ such that $k(x, y) \geq \varepsilon$ for all $x, y \in \mathbf{E}$.

$$\varepsilon := \min_{(x, y) \in \mathbf{E} \times \mathbf{E}} k(x, y) > 0.$$

Therefore, for any measurable $B \subseteq \mathbf{E}$ and all $x \in \mathbf{E}$,

$$K(x, B) = \int_B k(x, y) \psi(dy) \geq \int_B \varepsilon \psi(dy) = \varepsilon \psi(B), \quad (18)$$

which yields the desired petite set minorization $K(x, \cdot) \geq \varepsilon \psi(\cdot)$. Therefore, \mathbf{E} is a small set and using Lemmas C.3 and C.4, it is automatically petite. In our DDPM kernel, the Gaussian noise term ensures that the whole image cube is petite, even though it is uncountable. In other words, the whole cube $([0, 1]^{H \times W \times C})$ functions as a regeneration region, ensuring repeated access to the full state space.

Harris recurrent is the right notion of “will certainly return” for Markov chains in a general state space. If a Markov chain is ψ -irreducible, aperiodic, and has a petite set, then the chain is Harris recurrent (Meyn and Tweedie, 2nd edition, Theorem 9.1.7). We restate the theorem here and refer to the book for the proof.

Lemma C.5 (ψ -irreducible + aperiodicity + petite set \Rightarrow Harris recurrence). *Suppose that a Markov chain is ψ -irreducible, if there exists some petite set in $\mathcal{B}(\mathbf{E})$ such that the hitting probability $L(x, C) \equiv 1$, $x \in \mathbf{E}$, then the chain is Harris recurrent.*

In other words, if there is any petite set C that the chain is guaranteed to hit eventually, no matter where it starts, i.e., hitting probability $L(x, C) \equiv 1$ for every state x , then the whole chain is Harris recurrent. Harris recurrence requires that, relative to the same ψ , every set of positive ψ -measure is hit with probability 1 from every starting point.

²By contrast, a finite set only describes the number of elements; it does not guarantee such mixing. For instance, a finite set may fail to be petite if the chain gets trapped in an absorbing state, e.g. CycleGAN GMC

C.3.4 Ergodicity

We now complete the analysis of the generational Markov chain (GMC) by proving that the latent-feedback GMC is *ergodic*: irrespective of the starting state, it converges to a unique invariant distribution. We begin by recalling the relevant metric.

Definition 2 (Total variation (TV) norm ($\|\cdot\|_{TV}$)). *if μ is a signed measure on $\mathcal{B}(\mathbf{E})$, then the total variation norm $\|\mu\|$ is defined as*

$$\|\mu\| := \sup_{f:|f|\leq 1} |\mu(f)| = \sup_{A\in\mathcal{B}(\mathbf{E})} \mu(A) - \inf_{A\in\mathcal{B}(\mathbf{E})} \mu(A)$$

The total variation (TV) norm measures the maximum discrepancy between the probability measures. There are two equivalent ways to measure this total size: one is to see how large μ can be when integrated against any test function f with values between -1 and 1 ; equivalently, it measures the difference between the sets where the probability mass is maximally assigned and minimally assigned. The TV distance defined this way is a genuine metric between probability measures and always lies between 0 and 1 .

Recall from Lemma C.4 that the one-step density of the GMC satisfies a petite set condition (Eq. 18) for some $\varepsilon > 0$ and the σ -finite reference measure ψ . In combination with ψ -irreducibility (Lemma C.1), aperiodicity (Lemma C.2), and positive Harris recurrence (Lemma C.5), this is enough to establish ergodicity of the GMC.

Corollary 1 (Ergodic GMCs). *The generational Markov chain $\{X_n\}_{n\geq 0} : X_{n+1} \sim K(X_n, \cdot)$, with transition kernel K , is ergodic on state space $E \subset [0, 1]^{H\times W\times C}$ and have following properties:*

1. *Existence and uniqueness of the stationary law. If an ergodic Markov chain starts from an initial distribution $X_0 \sim \Pi_0$, it converges to a unique stationary distribution Π after mixing and this distribution π remains invariant under further application of the transition kernel K .*
2. *$K^n(x, \cdot)$ converges to π in total variation from a fixed starting point $x \in \mathbf{E}$ and $n \geq 0$,*

$$\lim_{n\rightarrow\infty} \|K^n(x, \cdot) - \pi\|_{TV} = 0, \quad \forall x \in \mathbf{E}. \quad (19)$$

Proof. ψ -irreducibility together with aperiodicity ensures that any two invariant probability measures must coincide (Meyn–Tweedie, Theorem 13.0.1), hence uniqueness once existence is shown. Positive Harris recurrence (Lemma 3.5) furnishes existence. \square

C.4 Empirical Analysis of GMCs

We empirically analyze both ergodic and non-ergodic GMCs. A chain is classified as ergodic if it satisfies three conditions: ψ -irreducibility, aperiodicity, and Harris recurrence. For our experiments—particularly in the context of iterative feedback for image generative models—the key requirement in practice is the one-step positive density condition, which ensures a non-zero probability of moving between any two states. In practice, this condition can be satisfied by sampling algorithms that incorporate an annealed Gaussian step (Gaussian noise step, Algo. 1). Conversely, any GMC that fails to meet one or more of the above conditions is non-ergodic.

C.4.1 Non-Ergodic GMCs

The construction of most iterative feedback-based image generative chains follows a common pattern: samples generated by the current model are used to train the next model. The functional analogue of Lucier’s feedback loop and CycleGAN chains fail this one-step density requirement, and thus are non-ergodic. Both systems instead behave like absorbing Markov chains with a finite set of states.

The functional analogue of Lucier’s feedback loop is modeled using a fixed room impulse response, which repeatedly applies convolution to its own output. As a result, the induced GMC lacks a positive transition probability from one state to any other. Similarly, the CycleGAN GMC exhibits the behavior of an absorbing Markov chain with multiple attractor states. During the cyclic translation process between domains, output images move from an attractor in one domain to the corresponding attractor in the other (Fig. 2 of the main paper).

Although they may appear stationary, these GMCs simply cycle among a finite set of absorbing states. Moreover, local and cumulative drifts could not be reliably estimated because outputs quickly drifted out-of-domain for their respective classifier networks.

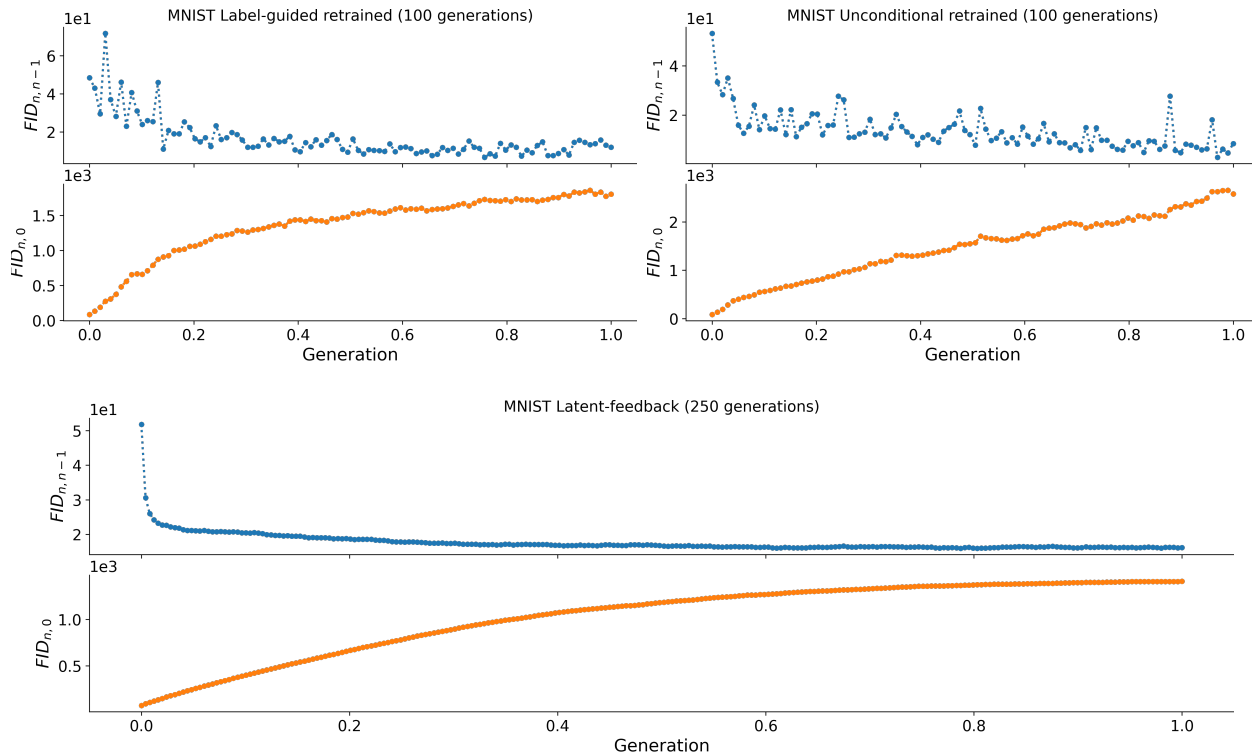


Figure 5: **Local and cumulative drifts in generational Markov chains on MNIST.** Each plot shows the local drift ($FID_{n,n-1}$, top) and cumulative drift ($FID_{n,0}$, bottom) across generations. Results are shown for the label-guided retrained diffusion model (top left), the unconditional retrained diffusion model (top right), and the latent-feedback diffusion model (bottom). Together they illustrate distinct convergence behaviors—rapid stabilization in the label-guided case, continued evolution in the unconditional model, and gradual stationarity in the latent-feedback chain.

C.4.2 Ergodic GMCs

All other GMCs in our diffusion-based framework—namely latent-feedback, label-guided retrained, and unconditional retrained—satisfy the critical one-step positive density condition and are therefore ergodic. Figures 5 and 6 present the local and cumulative drift plots for the corresponding experiments, with the number of generations scaled to a maximum of 1. We begin by discussing the MNIST-based experiments.

MNIST dataset: Fig. 5 tracks the local-drift indicator $FID_{n,n-1}$ (blue curve) and the cumulative-drift indicator $FID_{n,0}$ (orange curve) for the label-guided retrained, unconditional retrained, and latent-feedback GMCs.

In the label-guided retrained GMC (100 steps, Fig. 5 top-left-panel), the first ~ 40 iterations show an active transient phase (sharp local drift decrease and cumulative drift increase). Between steps 40-90, the system enters a slow transient phase, and by ~ 90 iterations both curves plateau, indicating empirical stationarity: the local drift plateaus, and the long-range distance ceases to grow. Here, the label-guidance signal reinforces this effect by anchoring each class manifold and preventing further cumulative drift, effectively keeping the distribution centered around class-conditional attractors.

For the *unconditional retrained* GMC with 100 iteration steps (Fig. 5, top-right panel), the local-drift curve (blue) drops sharply during the first 30 generations, after which the rate of decline slows to a small value. This indicates that each new generation still differs appreciably from its predecessor, with occasional spikes likely corresponding to mode-switching events. In contrast, the cumulative-drift curve (orange) rises almost linearly throughout the entire 100-step horizon, showing that the chain continues to move away from the original data manifold rather than settling into a stationary distribution. Taken together, a persistently high and fluctuating local drift, coupled with an unbounded cumulative drift, signals ongoing evolution.

In the *latent-feedback* GMC with 250 iteration steps (bottom panel of Fig. 5), the local-drift curve plunges during the first 20 iterations and then stabilizes at a small constant value. Meanwhile, the cumulative-drift curve rises steadily as the chain diverges from its initial distribution. During the first 100 iterations, the chain remains in an active transient

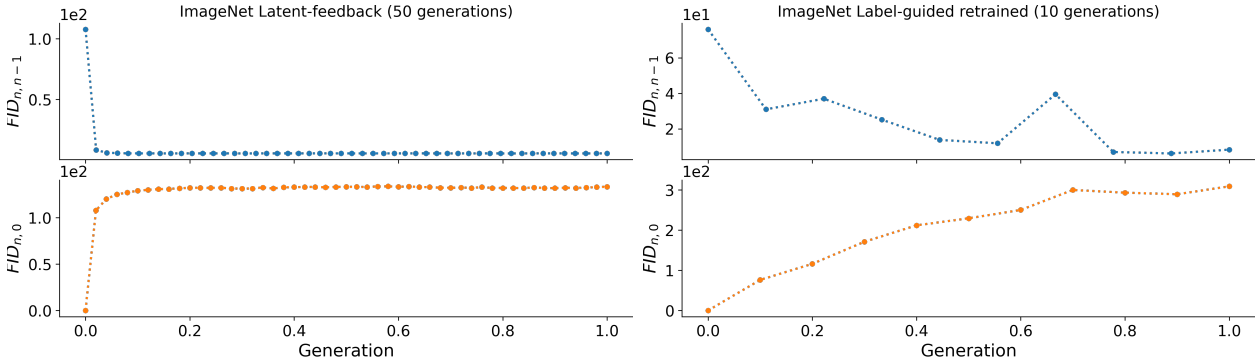


Figure 6: **Local and cumulative drifts in generational Markov chains on ImageNet-5.** Each plot displays the local drift ($FID_{n,n-1}$, top sub-panel) and the cumulative drift ($FID_{n,0}$, bottom sub-panel) across generations. Results are shown for the latent-feedback diffusion model (left) and the label-guided retrained diffusion model (right). Both chains stabilize quickly, highlighting how the complexity of the dataset can affect the behavior of the chain.

phase, followed by a slow transient phase for the next 100 iterations. Around the 200th iteration, the cumulative drift begins to taper off and eventually plateaus. This joint plateau pattern indicates empirical stationarity of the GMC.

ImageNet-5 dataset: We experiment with two GMCs—latent-feedback and label-guided retrained—on the ImageNet-5 dataset at $128 \times 128 \times 3$ resolution. The diffusion-based framework provides the theoretical foundation for one-step positive density in both GMCs.

For the *latent-feedback* GMC with 50 iteration steps, we use InceptionV3 features to provide latent feedback as conditional information in the diffusion process. Figure 6 (left) shows the drift plots for this GMC: the blue curve corresponds to local drift, and the orange curve to cumulative drift. Both curves change rapidly during the first few generations, followed by large plateaus that indicate empirical stationarity.

For the *label-guided retrained* GMC, we perform only 10 iterations since the outputs begin to lose semantic meaning in nearly all classes by the 5th generation. This is evident in the right panel of Figure 6, where the drift plots show sharp changes during the first few iterations and little to no change during the last three. Here, the GMC reaches its stationary distribution very quickly.

Across both GMCs, we observe that the chain converges to its stationary distribution within a few iterations. We posit that this behavior is influenced by the compressibility of the dataset: highly compressible images, such as MNIST digits, require only a small number of latent dimensions to faithfully represent the data, whereas ImageNet-5 images are far less compressible and demand significantly more dimensions to capture their semantic content (see global and local dimension plots in Figures 10 and 11). This suggests that the number of iterations required to reach a stationary distribution is closely tied to the compressibility of the dataset.

D Neural Resonance: Expanded

The convergence of a generational Markov chain toward a stationary distribution mirrors, in the statistical domain, the acoustic phenomenon in Alvin Lucier’s—*I Am Sitting in a Room*. In Lucier’s piece, successive re-recordings of a spoken passage act as repeated applications of the room’s linear transfer operator; frequencies misaligned with the dominant eigenmodes decay exponentially, leaving only the resonant “room chord.” Likewise, each iterative step of a diffusion-based Markov kernel suppresses components orthogonal to the data manifold, so that after a finite mixing time only those feature-space directions whose associated eigenvalues cluster near one—the stationary law—persist. The exponential fall-off in $FID_{n,n-1}$ thus plays the same diagnostic role as the narrowing audio spectrum in Lucier’s experiment: both quantify the attenuation of sub-dominant modes and provide an empirical estimate of the spectral gap. Framed in this way, ergodicity is not merely a probabilistic guarantee but a form of “*neural resonance*,” whereby low probability modes are filtered through successive generative iterations until the invariant statistical structure of the data reverberates alone, like the resonant frequencies of a physical room. Extending this fundamental principle beyond physical acoustics, we posit a direct conceptual analogy in generative neural networks, introducing the notion of *neural resonance*. We define:

Definition 3 (Neural resonance). *At the level of the entire data distribution, neural resonance denotes the emergence of a low-dimensional invariant subspace that is preserved under iterative generative updates.*

Table 3: **Latent-manifold dynamics under neural resonance.** Each row lists a distinct combination of directional change in the local spread (σ_{intra}), the local curvature measure (m_{LB}), and the global participation ratio (PR_G). Patterns are grouped into two regimes—semantic expansion (σ_{intra} increasing) and semantic contraction (σ_{intra} decreasing)—and each is labeled according to its geometric character (e.g., coherent expansion, wrinkled contraction). An animation illustrating these patterns is provided in the Supplementary Video.

| Manifold Behavior | | Local Metrics | | Global Metric | Dimensional Pattern |
|------------------------------------|-------------|------------------|----------|---------------|------------------------------|
| Local | Global | σ_{intra} | m_{LB} | PR_G | |
| Semantic Expansion Regime | | | | | |
| Expansion | Expansion | ↑ | ↑ | ↑ | Coherent Expansion (CE) |
| Expansion | Contraction | ↑ | ↑ | ↓ | Wrinkled Expansion (WE) |
| Expansion | Expansion | ↑ | ↓ | ↑ | Anisotropic Expansion (AE) |
| Expansion | Contraction | ↑ | ↓ | ↓ | Oblate Expansion (OE) |
| Semantic Contraction Regime | | | | | |
| Contraction | Contraction | ↓ | ↓ | ↓ | Coherent Contraction (CC) |
| Contraction | Expansion | ↓ | ↓ | ↑ | Anisotropic Contraction (AC) |
| Contraction | Contraction | ↓ | ↑ | ↓ | Wrinkled Contraction (WC) |
| Contraction | Expansion | ↓ | ↑ | ↑ | Oblate Contraction (OC) |

During convergence, the distribution variance projected onto directions orthogonal to this subspace decays exponentially, contracting its global effective dimensionality until it plateaus at the dimension of the resonant space. Concurrently, variance within that emerging subspace—such as intra-class spread—can transiently grow, shrink, or remain stable, modifying the local structure of the clusters without reversing the global collapse. Not every iterative-feedback generative model is guaranteed to exhibit neural resonance; it only shows when the two necessary conditions join forces:

- **Directional contraction:** Each iterative-feedback step steadily attenuates a broad set of latent-space directions globally, shrinking their influence bit by bit rather than leaving them unchanged.
- **Ergodicity:** No matter where the chain starts, its updates eventually explore a range of behaviors and head toward a stationary distribution.

When both conditions hold, modestly damped directions quickly fade, while nearly neutral directions retain the probability mass. The distribution therefore collapses onto a thin, lower-dimensional “resonant” sheet that remains stable under further iterations. When there is no directional contraction, the space never thins, and without ergodicity the generational chain can settle into disjoint attractors or drift without bound. Neural resonance pinpoints the regime in which global mixing and directional contraction cooperate to reveal—and continually reinforce—a persistent low-dimensional core, independent of how the chain began.

The resonance picture makes concrete, testable predictions about how *global* and *local* geometry evolve while the chain mixes. Globally, the participation ratio $PR_G(g)$ should decline monotonically until it plateaus at the dimension of the resonant subspace, signaling the collapse of variance in all orthogonal directions. Locally, however, the within-class spread $\sigma_{intra}(g)$ and the neighborhood embedding dimension $m_{LB}(g)$ can transiently increase, decrease, or remain stable as residual noise and semantic detail are funneled into the shrinking subspace. By tracking the joint trajectory $(\sigma_{intra}, m_{LB}, PR_G)$ we can understand the dynamics of the latent manifold, *how* intra-class spread reorganizes en route, and *which* latent-manifold regime—semantic expansion or contraction—dominates. The following subsection formalizes the eight qualitatively distinct sign-patterns that can arise.

D.1 Latent Manifold Dynamics: Expanded

We categorize the semantic phenomena according to their local impact on the latent manifold into two overarching regimes based on the increase and decrease in σ_{intra} : the *semantic-expansion* ($\sigma_{intra} \uparrow$) and the *semantic-contraction* ($\sigma_{intra} \downarrow$) regimes. Table 3 systematically catalogs every qualitatively distinct combination of local and global manifold behaviors. An animation illustrating the dimensional patterns is included in the supplementary video. Within the semantic expansion regime, the four rows describe the behavior of m_{LB} and PR_G with increase in σ_{intra} . Similarly, the semantic contraction regime enumerates behaviors of m_{LB} and PR_G for a decreasing σ_{intra} . Collectively, these eight sign-patterns ensure that any empirical latent-manifold trajectory can be classified and interpreted within this unified framework. We briefly describe the dimensional behavior of latent manifolds below:

- **Coherent Expansion** ($\sigma_{intra} \uparrow, \mathbf{m}_{LB} \uparrow, \mathbf{PR}_G \uparrow$): increase in σ_{intra} activates new axes of local variations, as evidenced by increase in m_{LB} . These new axes remain coherent across classes and align with the principal directions carrying significant global variance, increasing PR_G . Geometrically, the manifold simultaneously puffs out and unfolds into previously unoccupied subspaces, analogous to a balloon inflating so that new portions of its surface extend into directions that were previously unoccupied.
- **Wrinkled Expansion** ($\sigma_{intra} \uparrow, \mathbf{m}_{LB} \uparrow, \mathbf{PR}_G \downarrow$): increase in σ_{intra} forms small-scale ‘wrinkles’ or nonlinear creases within each cluster, increasing m_{LB} . However, these wrinkles do not align with the principal direction carrying significant global variance, effectively decreasing PR_G . Geometrically, the manifold fans out locally in new directions as wrinkles, creases or folds, but those directions cancel or average out globally, much like a sheet of fabric crumpling into many small folds that do not produce a consistent large-scale orientation.
- **Anisotropic Expansion** ($\sigma_{intra} \uparrow, \mathbf{m}_{LB} \downarrow, \mathbf{PR}_G \uparrow$): increase in σ_{intra} stretches each cluster anisotropically along different major axes, causing a decrease in m_{LB} . Nevertheless, this anisotropic stretching along different axes for different clusters activates additional global principal directions of significant variance, increasing PR_G . Thus, each cluster ‘grows out’ along its own axis—collapsing local dimensions while broadening the global footprint, much like lumps of play-dough being stretched in different directions, each elongating along its own axis while together occupying a wider region.
- **Oblate Expansion** ($\sigma_{intra} \uparrow, \mathbf{m}_{LB} \downarrow, \mathbf{PR}_G \downarrow$): increase in σ_{intra} expands the clusters along one or a few dominant directions, causing local clusters to oblate and collapse onto those axes, decreasing m_{LB} . Globally, the same (old) principal axes capture this increase in local variance, decreasing PR_G . The manifold oblates outward, similar to a balloon compressed between two plates, expanding sideways along a few axes while collapsing along others.
- **Coherent Contraction** ($\sigma_{intra} \downarrow, \mathbf{m}_{LB} \downarrow, \mathbf{PR}_G \downarrow$): This is the reverse of the *coherent expansion* process. The decrease in σ_{intra} removes new axes of local variations, decreasing m_{LB} . These disappearing local axes remain coherent across classes and align with the principal directions carrying significant global variance, decreasing PR_G .
- **Anisotropic Contraction** ($\sigma_{intra} \downarrow, \mathbf{m}_{LB} \downarrow, \mathbf{PR}_G \uparrow$): The dimensional pattern of anisotropic contraction is reverse of *wrinkled expansion* process. The decrease in σ_{intra} removes the ‘wrinkles’ or ‘nonlinear creases’ from the clusters converting into anisotropic cluster with different major axes. This local contraction decreases m_{LB} , but different clusters contract along distinct axes, activating new global principal directions of significant variance, increasing PR_G . In other words, each class shrinks along its own preferred axis anisotropically, causing the ensemble to diversify across more global modes despite overall contraction.
- **Oblate Contraction** ($\sigma_{intra} \downarrow, \mathbf{m}_{LB} \uparrow, \mathbf{PR}_G \uparrow$): The dimensional pattern of oblate contraction is the reverse of *oblate expansion* process. The decrease in σ_{intra} contracts the clusters along one or a few dominant directions, causing the local clusters to inflate along those axes, increasing m_{LB} . Globally, new principal directions capture this decrease in local variance, increasing PR_G .
- **Wrinkled Contraction** ($\sigma_{intra} \downarrow, \mathbf{m}_{LB} \uparrow, \mathbf{PR}_G \downarrow$): The dimensional pattern of the wrinkled contraction is the reverse of *anisotropic expansion* process. The decrease in σ_{intra} de-stretches each clusters creating wrinkles or nonlinear creases, increasing m_{LB} . Nevertheless, these de-stretching removes some of the previously required principal direction of variance, causing PR_G to decrease.

D.2 Dimensional Pattern of GMCs

To characterize the latent manifold dynamics of GMCs, we begin with low-dimensional projections (t-SNE) of their latent manifolds. These visualizations, see Fig. 7, reveal that different GMCs follow distinct evolutionary patterns, reflected in the organization and diffusion of clusters over time. Building on these observations, we then turn to a quantitative analysis of global (participation ratio) and local (Levina-Bickel intrinsic dimensionality) manifold behaviors. By tracking intra-class spread, intrinsic dimensionality, and participation ratio, we assign characteristic dimensional patterns discussed in Table 3 to different iterative phases of GMCs.

D.2.1 Low-Dimensional Projections of GMCs

To visualize the low-dimensional projections of GMCs in latent space, we compute a single t-SNE embedding jointly optimized with normalize perplexity and learning-rate across generation, ensuring comparability of all samples at each generation. t-SNE is a nonlinear dimensionality-reduction technique that maps high-dimensional data into two or three dimensions by converting pairwise similarities into joint probability distributions and then minimizing their Kullback-Leibler divergence [33]. Fig. 7 presents 2D t-SNE manifold projections for the three ergodic GMCs—latent-feedback, label-guided retrained, and unconditional-retrained—on the MNIST dataset. Each plot is computed from the

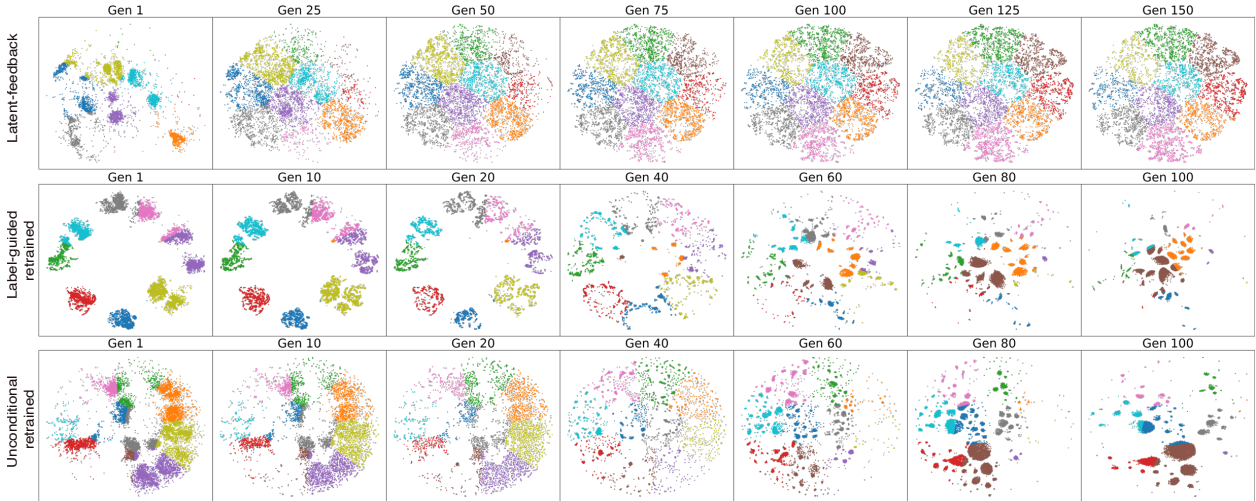


Figure 7: **t-SNE visualization of generational Markov chains on MNIST.** Each plot shows the two-dimensional t-SNE embedding of samples drawn from a generational Markov chain, grouped into ten clusters based on latent-space proximity rather than digit class. For the label-guided and unconditional retrained models, the first generation is trained on the MNIST training set and each subsequent generation uses 50,000 images. The latent-feedback chain starts from the MNIST test set, with 10,000 images per generation.

same latent-manifold activations used for other metric estimations. They are jointly estimated with identical perplexity and learning-rate settings. Even in two dimensions there is a clear indication of different GMCs following different dimensional patterns.

The *latent-feedback* GMC (top) begins with compact clusters that quickly diffuse into previously unoccupied regions, consistent with the early rise in σ_{intra} . The local expansion affects the local and global manifold dimension differently. The subspace stabilizes or evolves very slowly towards the end. The *label-guided retrained* GMC (middle) begins with sufficient cluster sizes for each class, but the clusters shrink without mixing with other classes (class-label acting as ‘anchors’, no sample from cluster boundaries), indicating a significant decrease in feature variance σ_{intra} around the middle generations. In later generations, σ_{intra} plateaus, indicating no significant change in distribution. The *unconditional-retrained* GMC (bottom) also starts with large clusters, but in the absence of class-label anchors, the clusters slowly shrink (decrease in σ_{intra}) and drift (with more samples from cluster boundaries appearing as incomplete digits) at the same time. As the GMC progresses, the distribution includes more incomplete digits, and digit 4 completely disappears from the sampled distribution around the 87th generation. This continues until the end of our experiment at the 100th generation.

Taken together, the t-SNE maps corroborate the quantitative curves: each GMC follows a distinct trajectory toward its stationary distribution, and changes in local spread (σ_{intra}) reshape both global and local latent-manifold geometry in different ways, consistent with the neural-resonance framework.

D.2.2 Global and Local Dimensions of GMCs

We track the dynamics of the latent-manifold of GMCs using intra-class spread σ_{intra} , intrinsic dimensionality m_{LB} , and participation ratio PR_G (discussed in Sec. B). We discuss the characteristics of the GMCs and interpret the manifold dynamics using the dimensional patterns described in Table 3 & Sec. D.1. To systematically analyze the dimensional patterns, we divide the whole iterative process into three phases—the *early* phase, the *middle* phase, and the *late* phase.

Lucier’s Feedback Loop We replicate a functional analogue of Lucier’s experiment on a recording of a reading of *War & Peace* using 10 different impulse responses from the OpenAIR dataset. We consider each impulse response as a class. This generation Markov chain does not have one-step positive density (Lemma C.1) and is not an ergodic GMC.

For latent-manifold tracking, we segmented each recording into non-overlapping partitions of 20 seconds and encoded every window with Wav2Vec 2.0 embeddings [34]. Fig. 8 charts the latent-manifold dynamics across iterations. The early phase shows *wrinkled-expansion* where both σ_{intra} and m_{LB} increase but PR_G decreases. The middle phase shows dynamics close to *oblate-expansion* behavior marked by slow increase of σ_{intra} , and a slow decrease of m_{LB} and PR_G . The late phase shows *wrinkled-contraction* marked by decrease in σ_{intra} and PR_G while m_{LB} increases.

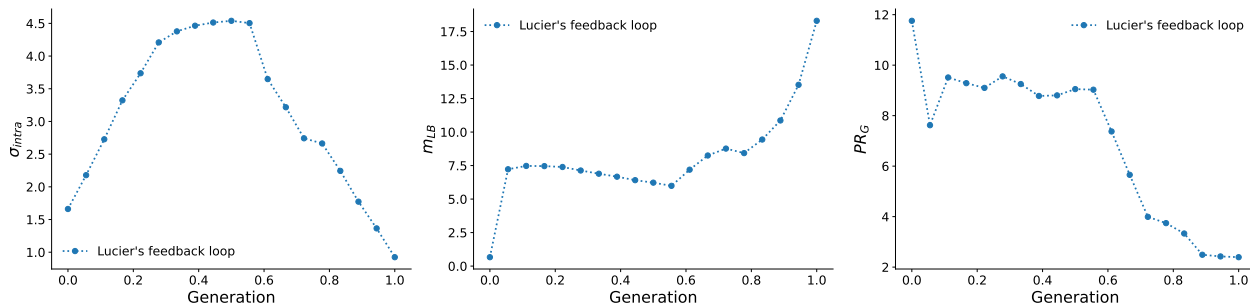


Figure 8: **Dimensional pattern of a functional analogue of Lucier’s feedback GMC.** We track the dimensional pattern of the GMC using three metrics— σ_{intra} , m_{LB} , and PR_G —computed in the Wav2Vec 2.0 latent space for an audiobook of *War and Peace* convolved with OpenAIR impulse-response signals. In the early phase the latent manifold undergoes a wrinkled expansion, followed by an oblate expansion in the middle phase, and a wrinkled contraction in the final phase, nearly reducing PR_G to zero and driving m_{LB} to very large values. The chain does not exhibit neural resonance.

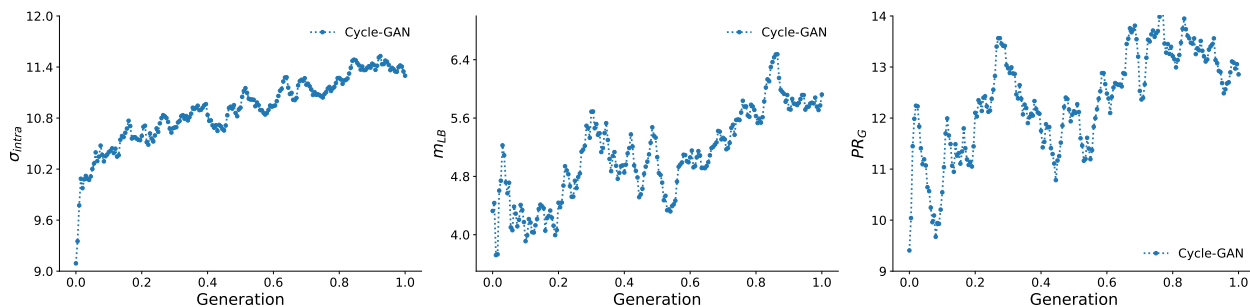


Figure 9: **Dimensional pattern of CycleGAN GMC** From left to right, the plot tracks intra-class spread, local and global dimensions on Horse-Zebra dataset for 200 iterations.

Despite the sustained directional contraction in the neural or embedding space, the functional analogue of Lucier’s experiment does not show neural resonance—the original physical experiment does exhibit acoustic resonance—because the corresponding GMC is non-ergodic.

Cyclic Image Translation We apply CycleGAN to the Horse-Zebra corpus, yielding a fully deterministic transformation operator. Because the update map lacks a one-step positive density (Lemma C.1), the associated generative Markov chain is non-ergodic: it does not mix toward a stationary distribution but instead settles into a limit cycle governed by the reconstruction loss and the two image domains.

Latent-manifold dynamics are tracked with features from the penultimate layer of a pretrained Inception-V3 encoder. Fig. 9 reports the three metrics over 200 iterations. Generation-to-generation behavior is irregular—each generator repeatedly attempts to undo its counterpart’s output—but the aggregate trend resembles a *coherent-expansion*: the within-class spread σ_{intra} , the local dimensionality m_{LB} , and the global participation ratio PR_G all increase. Because neither global contraction nor mixing is observed, this CycleGAN chain never enters the neural-resonance regime.

Latent-Feedback Diffusion Models We run latent-feedback experiments with diffusion models on the MNIST and ImageNet-5 datasets. Because a diffusion step admits a one-step positive density (Lemma C.1) and the resulting feedback chain also meets the criteria of local self-transition, petite sets, and Harris recurrence (Lemmas C.2–C.5), the associated generative Markov chain is ergodic. Given enough feedback iterations, it should therefore mix toward a stationary distribution.

For the MNIST experiment we monitor latent-manifold dynamics over 250 feedback iterations using features from a pretrained classifier. Fig. 10 (blue curve) shows the first 100 iterations, after which the behavior remains qualitatively unchanged. Throughout, the latent-feedback chain exhibits an *oblate-expansion* pattern: the within-class spread σ_{intra} rises early and then plateaus, while both the local dimensionality m_{LB} and the global participation ratio PR_G contract steadily before stabilizing at a fixed value. Because the process satisfies ergodicity and displays strong directional contraction, it meets the two criteria for neural resonance.

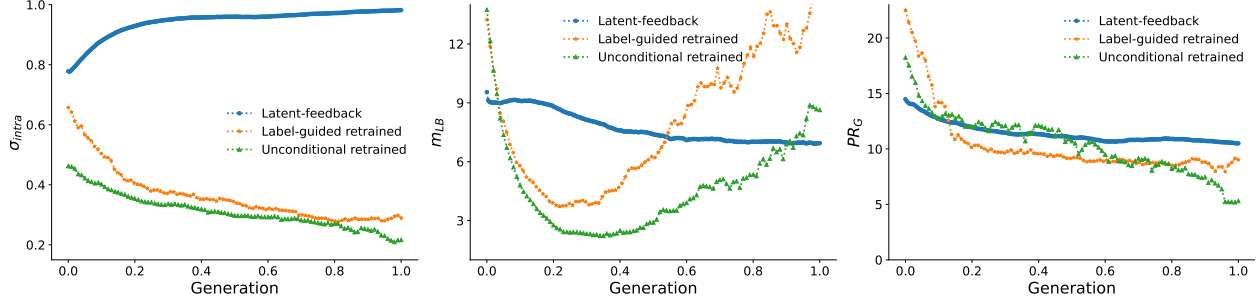


Figure 10: **Dimensional pattern of GMCs on MNIST dataset.** From left to right, the plot tracks intra-class spread, local and the global dimensions of latent-feedback (blue, 200 iterations), label-guided retrained (orange, 100 iterations) and unconditional retrained (green, 100 iterations) GMCs.

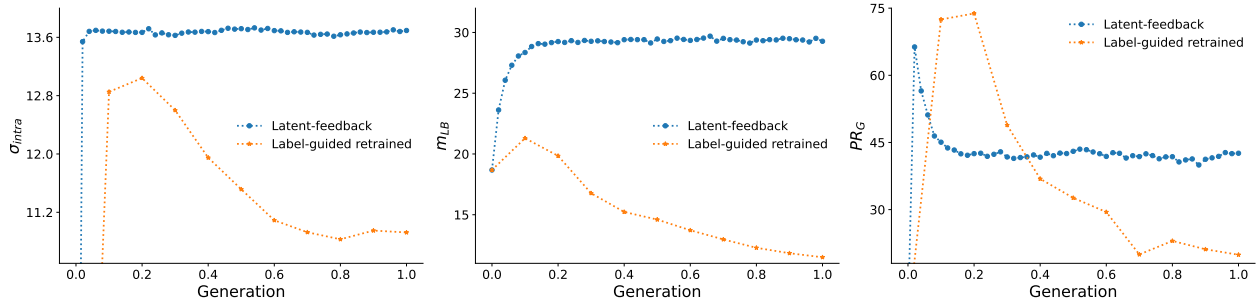


Figure 11: **Dimensional pattern of GMCs on ImageNet-5 dataset.** From left to right, the plot tracks intra-class spread, intrinsic dimensionality and global dimensions of the latent-feedback (blue, 50 iterations) and label-guided retrained (orange, 11 iterations) diffusion models.

For the ImageNet-5 latent-feedback chain we monitored manifold evolution using features from the penultimate layer of a pretrained Inception-V3 encoder. Fig. 11 (blue curve) depicts the first 50 feedback iterations. In the early stages both the within-class spread σ_{intra} and the local intrinsic dimensionality m_{LB} rise before leveling off, while the global participation ratio PR_G collapses rapidly and then plateaus. This combination—local variance inflating inside a concurrently shrinking global subspace—matches the *wrinkled-expansion* regime. Because the chain is ergodic and displays strong directional contraction, it satisfies the two conditions required for neural resonance.

Label-Conditional Retrained Diffusion Models We run label-conditional retrained model experiments with diffusion models on the MNIST and ImageNet-5 datasets. These GMCs are also ergodic satisfying Lemmas C.1-C.5. Given enough feedback iterations, it should therefore mix towards a stationary distribution.

In the MNIST study we track the generative Markov chain for 100 feedback iterations; its latent-manifold trajectory is plotted as the orange curve in Fig. 10. During the initial iterations the chain undergoes a pronounced *coherent-contraction*: all three metrics—within-class spread σ_{intra} , local dimension m_{LB} , and global participation ratio PR_G —fall sharply. From the middle phase onward, m_{LB} begins a gradual rebound while σ_{intra} and PR_G stabilize or continue to decline, marking a transition to *wrinkled-contraction*. Because the chain is ergodic and exhibits sustained directional damping, it fulfills the two criteria required for neural resonance.

In the ImageNet-5 experiment we track the chain for only ten feedback iterations; the orange curve in Fig. 11 reveals an aggressive, monotonic decline in all three manifold metrics. By iteration 10 the outputs have deteriorated to near-random noise with only faint object silhouettes remaining. The chain nevertheless remains ergodic and exhibits rapid directional contraction, thereby satisfying the prerequisites for neural resonance.

Unconditional Retrained Diffusion Model We evaluate the unconditional retrained diffusion model solely on the MNIST dataset. Like the latent-feedback and label-guided variants, this chain possesses a positive one-step density and satisfies the petite-set and Harris-recurrence conditions, making it ergodic; with sufficient iterations it should therefore converge to a stationary distribution.

The chain is run for 100 feedback steps, with each batch re-classified by a pretrained digit classifier before manifold analysis. The green curve in Fig. 10 summarizes its trajectory: the within-class spread σ_{intra} and the global

participation ratio PR_G fall almost linearly, while the intrinsic dimensionality m_{LB} drops sharply at first and then rebounds slightly. Although the process meets both prerequisites for neural resonance—ergodicity and sustained directional contraction—the characteristic resonant plateau (see Fig.5 top right panel) has not yet appeared. This is also evident in the PR_G plot, where the global dimensionality continues to contract without showing signs of stabilization within the first 100 iterations.

E Discussion

Our study offers a unified theoretical and empirical perspective on how generational Markov chains (GMCs)—iterative models that recycle their own outputs—evolve in latent space. By treating examples as diverse as the functional analogue of Lucier’s acoustic feedback loop, CycleGAN image translation, latent-feedback diffusion sampling, and both unconditional and label-guided retraining models, we derive general conditions under which a GMC is *ergodic*. To assess its empirical stationarity, we introduce two complementary FID traces: $FID_{n,n-1}$, which serves as a *local-drift* indicator, and $FID_{n,0}$, which acts as a *cumulative-drift* indicator. When both metrics change rapidly the chain is in an *active-transient* phase; when one curve evolves slowly while the other has flattened, the system is in a *slow-transient* phase; and when both traces plateau simultaneously, the GMC has reached empirical stationarity.

Drawing inspiration from Alvin Lucier’s original experiment, which exhibits acoustic resonance (but our functional analogue lacks ergodicity, hence no neural resonance), and examining our formulation of GMCs across diverse settings, we identified an analogous phenomenon in latent feature space, which we term *neural resonance*. Two conditions are necessary for its emergence: (i) *ergodicity*, which guarantees convergence to a stationary distribution, and (ii) *directional contraction*, which drives variance in non-resonant directions toward zero. When both criteria are met, the GMC collapses onto a low-dimensional, update-invariant subspace; when either is violated, the chain either cycles within a finite set of attractors (as in CycleGAN image translation) or drifts without bound. We link this theory to three empirical manifold metrics— σ_{intra} , m_{LB} , and PR_G —whose joint trajectories reveal eight characteristic dimensional patterns in latent space. Together, these measures form a compact yet powerful toolkit for diagnosing the dynamics of iterative generative systems.

Several caveats temper these findings. All quantitative metrics were extracted in fixed feature spaces (Inception-V3 for images and Wav2Vec 2.0 for audio); the absolute plateau heights of the drift curves therefore depend on the specific embedding. The benchmark suites employed here, MNIST, ImageNet-5, and OpenAIR, are modest in scale compared with contemporary foundation models, so the interplay between neural resonance and transformer-sized architectures remains an open research question.

We highlight two directions for future exploration. (i) *Mitigation*. Designing noise schedules or regularizers that either delay or suppress generational collapse without sacrificing sample fidelity. (ii) *Cross-modal generalization*. Extending the resonance framework to text-only and vision-language models, where directional contraction must be defined in semantic rather than pixel space.

In summary, the combination of Markov-chain theory and feature-space geometry presented in this work provides a principled lens through which to analyze—and ultimately control iteratively trained generative models. The empirical signatures introduced here should enable practitioners to detect generational collapse at an early stage and intervene before complete collapse of diversity. As generative AI systems assume ever more autonomous roles, such safeguards will be essential for preserving fidelity, variety, and, ultimately, trustworthiness in their outputs.

References

- [1] Karl Johan Astrom and Richard M. Murray. *Feedback Systems: An Introduction for Scientists and Engineers*. Princeton University Press, USA, 2008.
- [2] Ilia Shumailov, Zakhar Shumaylov, Yiren Zhao, Nicolas Papernot, Ross Anderson, and Yarin Gal. Ai models collapse when trained on recursively generated data. *Nature*, 631(8022):755–759, 2024.
- [3] Alvin Lucier and Douglas Simon. I am sitting in a room. -, 1969.
- [4] Sean Meyn and Richard L. Tweedie. *Markov Chains and Stochastic Stability*. Cambridge University Press, USA, 2nd edition, 2009.
- [5] Elizaveta Levina and Peter J. Bickel. Maximum likelihood estimation of intrinsic dimension. In *Advances in Neural Information Processing Systems 17*, pages 777–784, Cambridge, MA, 2005. MIT Press.
- [6] Jonathan S Abel and Michael J Wilson. Luciverb: Iterated convolution for the impatient. In *Audio Engineering Society Convention*, volume 133, 2012.

- [7] Jun-Yan Zhu, Taesung Park, Phillip Isola, and Alexei A Efros. Unpaired image-to-image translation using cycle-consistent adversarial networks. In *Proceedings of the IEEE International Conference on Computer Vision (ICCV)*, pages 2223–2232, 2017.
- [8] David C. Carslaw and Karl Ropkins. openair — an r package for air quality data analysis. *Environmental Modelling and Software*, 27–28(0):52–61, 2012.
- [9] Prafulla Dhariwal and Alexander Nichol. Diffusion models beat gans on image synthesis. *Advances in neural information processing systems*, 34:8780–8794, 2021.
- [10] Elvis Dohmatob, Yunzhen Feng, Pu Yang, Francois Charton, and Julia Kempe. A tale of tails: model collapse as a change of scaling laws. ICML’24, Vienna, Austria, 2024. JMLR.org.
- [11] Yanzhu Guo, Guokan Shang, Michalis Vazirgiannis, and Chloé Clavel. The curious decline of linguistic diversity: Training language models on synthetic text. In Kevin Duh, Helena Gomez, and Steven Bethard, editors, *Findings of the Association for Computational Linguistics: NAACL 2024*, pages 3589–3604, Mexico City, Mexico, June 2024. Association for Computational Linguistics.
- [12] Martin Briesch, Dominik Sobania, and Franz Rothlauf. Large language models suffer from their own output: An analysis of the self-consuming training loop, 2024.
- [13] Sina Alemohammad, Josue Casco-Rodriguez, Lorenzo Luzi, Ahmed Imtiaz Humayun, Hossein Babaei, Daniel LeJeune, Ali Siahkoobi, and Richard Baraniuk. Self-consuming generative models go MAD. In *The Twelfth International Conference on Learning Representations*, 2024.
- [14] Matthias Gerstgrasser, Rylan Schaeffer, Apratim Dey, Rafael Rafailov, Tomasz Korbak, Henry Sleight, Rajashree Agrawal, John Hughes, Dhruv Bhandarkar Pai, Andrey Gromov, Dan Roberts, Diyi Yang, David L. Donoho, and Sanmi Koyejo. Is model collapse inevitable? breaking the curse of recursion by accumulating real and synthetic data. In *First Conference on Language Modeling*, 2024.
- [15] Ryuichiro Hataya, Han Bao, and Hiromi Arai. Will large-scale generative models corrupt future datasets? In *Proceedings of the IEEE/CVF International Conference on Computer Vision (ICCV)*, pages 20555–20565, October 2023.
- [16] Maty Bohacek and Hany Farid. Nepotistically trained generative image models collapse. In *ICLR 2025 Workshop on Navigating and Addressing Data Problems for Foundation Models*, 2023.
- [17] Quentin Bertrand, Avishek Joey Bose, Alexandre Duplessis, Marco Jiralerspong, and Gauthier Gidel. On the stability of iterative retraining of generative models on their own data. In *ICLR*, 2024.
- [18] Youngseok Yoon, Dainong Hu, Iain Weissburg, Yao Qin, and Haewon Jeong. Model collapse in the self-consuming chain of diffusion finetuning: A novel perspective from quantitative trait modeling. In *ICLR 2025 Workshop on Navigating and Addressing Data Problems for Foundation Models*.
- [19] Nate Gillman, Michael Freeman, Daksh Aggarwal, Chia-Hong Hsu, Calvin Luo, Yonglong Tian, and Chen Sun. Self-correcting self-consuming loops for generative model training. In *Proceedings of the 41st International Conference on Machine Learning*, ICML’24, Vienna, Austria, 2024. JMLR.org.
- [20] Lianghe Shi, Meng Wu, Huijie Zhang, Zekai Zhang, Molei Tao, and Qing Qu. A closer look at model collapse: From a generalization-to-memorization perspective. In *The Impact of Memorization on Trustworthy Foundation Models: ICML 2025 Workshop*, 2025.
- [21] Rohan Taori and Tatsunori Hashimoto. Data feedback loops: Model-driven amplification of dataset biases. In Andreas Krause, Emma Brunskill, Kyunghyun Cho, Barbara Engelhardt, Sivan Sabato, and Jonathan Scarlett, editors, *Proceedings of the 40th International Conference on Machine Learning*, volume 202 of *Proceedings of Machine Learning Research*, pages 33883–33920, July 2023.
- [22] Shi Fu, Sen Zhang, Yingjie Wang, Xinmei Tian, and Dacheng Tao. Towards theoretical understandings of self-consuming generative models. In *Proceedings of the 41st International Conference on Machine Learning*, ICML’24, Vienna, Austria, 2024. JMLR.org.
- [23] Yann LeCun, Corinna Cortes, and CJ Burges. Mnist handwritten digit database. *ATT Labs [Online]*. Available: <http://yann.lecun.com/exdb/mnist>, 2, 2010.
- [24] Olga Russakovsky, Jia Deng, Hao Su, Jonathan Krause, Sanjeev Satheesh, Sean Ma, Zhiheng Huang, Andrej Karpathy, Aditya Khosla, Michael Bernstein, et al. Imagenet large scale visual recognition challenge. *International Journal of Computer Vision*, 115(3):211–232, 2015.
- [25] Leo Tolstoy. War and Peace: Audiobook. Audio recording, read by Neville Jason. Internet Archive. <https://archive.org/details/03Disc30f4>, June 2018. Uploaded by kazanfrog.

- [26] Martin Heusel, Hubert Ramsauer, Thomas Unterthiner, Bernhard Nessler, and Sepp Hochreiter. Gans trained by a two time-scale update rule converge to a local nash equilibrium. NIPS'17, page 6629–6640, Red Hook, NY, USA, 2017. Curran Associates Inc.
- [27] R.A. Fisher. The use of multiple measurements in taxonomic problems. *Annals of Eugenics*, 7(2):179–188, 1936.
- [28] Thomas C. Halsey, Mogens H. Jensen, Leo P. Kadanoff, Itamar Procaccia, and Boris I. Shraiman. Fractal measures and their singularities: the characterization of strange sets. *Physical Review A*, 33(2):1141–1151, 1986.
- [29] Jean-Pierre Eckmann and David Ruelle. Multifractal measures and their singularities: The characterization of strange sets. *Communications in Mathematical Physics*, 99(1):123–153, 1988.
- [30] Jonathan Ho, Ajay Jain, and Pieter Abbeel. Denoising diffusion probabilistic models. *Advances in neural information processing systems*, 33:6840–6851, 2020.
- [31] Yang Song and Stefano Ermon. *Generative modeling by estimating gradients of the data distribution*. Curran Associates Inc., Red Hook, NY, USA, 2019.
- [32] Yang Song, Jascha Sohl-Dickstein, Diederik P Kingma, Abhishek Kumar, Stefano Ermon, and Ben Poole. Score-based generative modeling through stochastic differential equations. In *Proceedings of the International Conference on Learning Representations (ICLR)*, 2021.
- [33] Laurens van der Maaten and Geoffrey Hinton. Visualizing data using t-sne. *Journal of Machine Learning Research*, 9(86):2579–2605, 2008.
- [34] Alexei Baevski, Yuhao Zhou, Abdelrahman Mohamed, and Michael Auli. wav2vec 2.0: A framework for self-supervised learning of speech representations. *Advances in neural information processing systems*, 33:12449–12460, 2020.